

**COMBINED THEORETICAL AND
EXPERIMENTAL STUDY OF
CO ADSORPTION AND REACTIVITY OVER
PLATINUM AND COBALT**

**GOVINI THANTHRIGE KASUN KALHARA
GUNASOORIYA**

NATIONAL UNIVERSITY OF SINGAPORE

2014

**COMBINED THEORETICAL AND
EXPERIMENTAL STUDY OF
CO ADSORPTION AND REACTIVITY OVER
PLATINUM AND COBALT**

**GOVINI THANTHRIGE KASUN KALHARA
GUNASOORIYA**

B.Eng(Chemical Engineering)(Hons), NUS

A THESIS SUBMITTED

FOR THE DEGREE OF MASTER OF ENGINEERING

**DEPARTMENT OF CHEMICAL & BIOMOLECULAR
ENGINEERING**

NATIONAL UNIVERSITY OF SINGAPORE

2014

Declaration

I hereby declare that this thesis is my original work and it has been written by me in its entirety. I have duly acknowledged all the sources of information which have been used in this thesis.

This thesis has also not been submitted for any degree in any university previously.

Govini Thantrige Kasun Kalhara Gunasooriya

21 August 2014

Acknowledgements

I sincerely thank my supervisor, Professor Mark Saeys, for his insights, encouragement, and incessant guidance throughout the course. He initiated me to the field of first principle studies and gave me the opportunity to work under the project funded by Shell Global Solutions. I am grateful for his availability, sharing his broad and profound knowledge with me and fuelling my curiosity. I am also inspired by his high integrity and dedication in the scientific research.

I am grateful for colleagues at Shell Global Solutions, Dr. Sander van Bavel, Dr. Herman Kuipers, Dr. Rajappan Vetrivel, Dr Leonardo Spanu for all the insightful discussions. I am also grateful for, Dr. Chen Luwei, Dr. Daniel Ong, Dr. Poh Chee Kok and staff at the Institute for Chemical Engineering Science (Jurong Island, Singapore) for guiding me in my experimental studies.

The Saeys group has been a wonderfully diverse and fun research group to be in. I owe thanks to Dr. Zhou Mingkun and Dr Gavin Chua Yong Ping for their guidance in the initial stages. Special thanks to Arghya for his friendship, the meals, the cricket, the trips and light-hearted banter about everyday life to thought provoking discussions on politics. I would also like to thank all my colleagues, Thang, Novi, Tiangyang, Jensen, Yi Rui and all the FYP/summer undergrads for your presence and friendship in the group.

I am blessed to be with a wonderful and supportive family. I am thankful for my parents and my lovely sister who have always stood by me and encouraged me to give my best throughout this journey. Amma, Thaththa and Nangi, thank you for everything. Most importantly, my dear Grace, you are the most beautiful thing that has ever happened to me. You have always been by my side during the good times and bad. Thank you for your love, patience and understanding.

And above all, I would like thank God for His abundant love and grace for providing me strength throughout this journey. (Philippians 4:13)

Table of Contents

| | |
|--|-------|
| Declaration..... | I |
| Acknowledgements..... | II |
| Table of Contents..... | III |
| Summary..... | VI |
| List of tables..... | IX |
| List of figures..... | XI |
| Symbols and Abbreviations..... | XVI |
| Publications..... | XVIII |
| | |
| 1 Introduction..... | 1 |
| 1.1 CO adsorption on transition metal surfaces..... | 2 |
| 1.1.1 Experimental studies..... | 2 |
| 1.1.2 Theoretical studies..... | 5 |
| 1.1.3 Bonding of CO on transition metal surfaces..... | 6 |
| 1.2 Tuning catalytic activity via the Schwab effect..... | 11 |
| 1.2.1 Schwab effect..... | 11 |
| 1.2.2 Tuning the CO oxidation rate over Pt/TiO ₂ catalysts by defect engineering of the TiO ₂ support..... | 13 |
| 1.3 Thesis structure..... | 15 |
| 1.4 References..... | 17 |
| | |
| 2 Computational method and models..... | 20 |
| 2.1 Density Functional Theory..... | 20 |
| 2.2 Catalyst models..... | 21 |
| 2.2.1 Cobalt catalyst models..... | 21 |
| 2.2.2 Platinum catalyst models..... | 22 |
| 2.3 VASP calculations..... | 23 |
| 2.3.1 Adsorption energy..... | 25 |
| 2.3.2 Gibbs Free energy..... | 26 |
| 2.3.3 Bader Charge..... | 29 |

| | |
|--|----|
| 2.3.4 Natural Bond Orbitals..... | 29 |
| 2.4 References | 31 |
| | |
| 3 CO adsorption on Cobalt: first principle prediction of a first order phase transition | 33 |
| 3.1 Introduction | 33 |
| 3.2 Results and discussions | 37 |
| 3.2.1 Low coverage CO adsorption | 37 |
| 3.2.2 High coverage CO adsorption | 44 |
| 3.2.3 CO adsorption Gibbs free energy diagram | 45 |
| 4.3 Conclusions | 50 |
| | |
| 4 CO adsorption on platinum: accurate prediction of site preference and analysis of the change in site preference at high coverage | 53 |
| 4.1 Introduction | 53 |
| 4.2 Results and discussions | 62 |
| 4.2.1 Low coverage CO adsorption | 62 |
| 4.2.2 High coverage CO adsorption | 66 |
| 4.2.3 Stability diagram for CO adsorption Pt(111) | 70 |
| 4.2.4 Change in relative stability of on-top CO vs bridge CO with coverage..... | 71 |
| 4.3 Conclusions | 78 |
| 4.4 References | 79 |
| | |
| 5 Analysis of the change in the CO oxidation rate over Pt clusters by changing the charge transfer from the TiO ₂ Anatase support | 82 |
| 5.1 Introduction | 82 |
| 5.2 Computational methods..... | 86 |
| 5.3 Computational results..... | 87 |
| 5.4 Conclusions | 92 |
| 5.5 References | 93 |

| | |
|--|----|
| 6 Conclusions and future work | 94 |
| 6.1 Thesis conclusions..... | 94 |
| 6.2 Suggestions for future work | 97 |
| 6.2.1 CO adsorption on other transition metals | 97 |
| 6.2.2 Tuning the ethylene hydrogenation rate over Pt/Anatase catalysts via the Schwab effect..... | 97 |
| 6.3 References | 99 |

Summary

The hydrogenation and oxidation of carbon monoxide (CO) over transition metal catalysts are arguably the most widely studied catalytic reactions, both experimentally and theoretically. The catalytic oxidation of CO over automotive exhausts catalysts and Fischer Tropsch synthesis to convert syngas, a mixture of carbon monoxide (CO) and hydrogen (H₂), to long chain hydrocarbons are some examples. Moreover, due to its simple structure and experimentally well studied adsorption properties, CO is generally used as a probe molecule in surface science. Catalytic reactions start by adsorbing CO onto the catalyst surface. In this thesis, the adsorption of CO on cobalt and platinum terraces was studied using state-of-the-art density functional theory (DFT) using the revised Perdew-Burke-Ernzerhof functional and including non-local vdW-DF correlation for a wide range of coverages. This new method shows surprising promise for the important catalyst systems studied here.

First, CO adsorption on hcp Co(0001) terraces was studied. Our approach, correctly predicts the preferred adsorption at the top as well as accurate adsorption energies, a long standing challenge for DFT. Moreover, only two stable surface structures or phases were found. All the other structures are significantly less stable. The stable structures are a low coverage $(\sqrt{3}\times\sqrt{3})R30^\circ$ -CO phase and a high coverage $(2\sqrt{3}\times 2\sqrt{3})R30^\circ$ -7CO phase,

separated by a first order-phase transition. The temperature and pressure of the first-order phase transition agree surprisingly well with available experimental data. The stability of the various surface structures was analyzed using the changes in the occupancies of the natural bond orbitals, a method to generate approximate localized Lewis-like structures from a delocalized quantum-chemical wave function and give insight into chemical bonding. This was recently extended to solid state structures and surfaces by the group of Schmidt in Wisconsin. Experimentally, phase transitions are characterized by a discontinuity in the physical properties and modern micro-calorimetric methods might hence be able to directly experimentally observe the predicted phase transition.

The situation is very different on the well-studied Pt(111) surface. Many surface structures have comparable stabilities and even for a given coverage, many competing structures exist. About 20 structures were evaluated and for example different stable structures with long-range order were found for 0.5 ML $\{(4 \times 2)\text{-}4\text{CO}$ or $(\sqrt{3} \times 2)\text{rect-}2\text{CO}\}$, 0.6 ML $\{(\sqrt{3} \times 5)\text{rect-}6\text{CO}\}$, 0.67 ML $\{(\sqrt{3} \times 3)\text{rect-}4\text{CO}\}$ based on the stability diagram. At low coverage, the adsorption energy at the top site, -143 kJ/mol, is 7 kJ/mol stronger than at the bridge site, in agreement with an estimate based on detailed simulations of experimental data. As the coverage increases, the difference between the top and bridge stability reduces, e.g., to while it is 7 kJ/mol at 0.125 ML, it reverses to -2 kJ/mol 0.25 ML. The change in the relative stability for the top and bridge sites was again analysed using the occupancies of the natural bond orbitals. For both the top and the bridge site Lewis structures with filled 2-

center orbitals (>1.9) were found, however, anti-bonding orbitals also have significant occupancies (>0.1) corresponding to Pauli repulsion. Reduced electron density at the bridge site Pt atoms, reduces Pauli repulsion, and increases the stability of CO at those sites.

Finally, to elucidate the gradual variation in the CO oxidation activity over sub-1 nm Pt clusters when the carrier density of the TiO₂ support is gradually changed (known as the Schwab effect), the effect of charge transfer to Pt on the CO adsorption energy was studied in detail. Our calculations together with a natural bond orbital analysis demonstrate that charge injection into the Pt particles reduces the CO adsorption energy by increasing the Pauli repulsion between the filled CO 5σ and the Pt d_{z^2} orbitals, consistent with the trends in the measured reaction rates.

List of tables

| | | |
|-----------|---|----|
| Table2.1 | Top view of the five different unit cells considered in chapter 3 of this thesis; $p(3 \times 3)$, $p(2\sqrt{3} \times 2\sqrt{3})$ unit cells. | 21 |
| Table2.2 | Top view of the five different unit cells considered in the chapter 4 of this thesis; $p(3 \times 3)$, $p(4 \times 2)$, $(\sqrt{3} \times 2)$, $(\sqrt{3} \times 5)$ and $(\sqrt{3} \times 4)$ unit cells. | 22 |
| Table 3.1 | Average and differential ^a CO adsorption energies, average Gibbs free adsorption energies (300 K, 1 mbar CO) (kJ/mol) and average entropy (J/mol K) of adsorbed CO for different configurations and coverages on Co(0001). | 38 |
| Table 3.2 | Average CO adsorption energy (kJ/mol), C-O and Co-C distances (Å), CO stretch frequency (cm^{-1}), occupancy of the anti-bonding Co-C NBO and of the C-O $2\pi^*$ NBO for key CO structures on Co(0001). | 41 |
| Table 4.1 | Average CO adsorption energies (kJ/mol), average Gibbs free adsorption energies (300 K, 1 mbar CO) (kJ/mol) and average entropy (J/mol K) for different low coverage configurations on a 5-layer Pt(111) slab with a $p(3 \times 3)$ unit cell. | 63 |
| Table 4.2 | C-O and Pt-C bond lengths (Å), CO stretch frequency (cm^{-1}), occupancy of the anti-bonding Pt-C NBO and of the C-O $2\pi^*$ NBO for key CO structures on Pt(111)- $p(3 \times 3)$ unit cell. | 65 |
| Table 4.3 | Average CO adsorption energies (kJ/mol), average Gibbs free adsorption energies (300 K, 1 mbar) (kJ/mol), and average entropy of adsorbed CO (J/mol K) for different configurations in a $c(4 \times 2)$ unit cell. | 66 |
| Table 4.4 | Average CO adsorption energies (kJ/mol), average Gibbs free adsorption energies (300 K, 1 mbar) (kJ/mol), and | 67 |

entropy of adsorbed CO (J/mol K) for different combinations of bridge and top sites in a ($\sqrt{3}\times 5$)rect unit cell, 0.6 ML.

| | | |
|-----------|--|----|
| Table 4.5 | Average CO adsorption energy (kJ/mol), average Gibbs free adsorption energy (300 K, 1 mbar) (kJ/mol) and entropy of adsorbed CO (J/mol K) for a 0.66 ML coverage in a ($\sqrt{3}\times 3$)rect unit cell. | 68 |
| Table 4.6 | Average CO adsorption energy (kJ/mol), average Gibbs free adsorption energy (300 K, 1 mbar) (kJ/mol) and entropy of adsorbed CO (J/mol K) for a 1 ML coverage in a ($\sqrt{3}\times 3$)rect unit cell. | 69 |
| Table 4.7 | Average and differential ^a CO adsorption energies adsorption energies, occupancy of the anti-bonding Pt-C NBO and of the C-O $2\pi^*$ NBO for 1/10 ML and 6/10 ML coverage CO structures on Pt(111)-($\sqrt{3}\times 5$)rect unit cell. | 75 |
| Table 4.8 | Low coverage DFT-revPBE-vdW-DF CO adsorption energy as the charge of the surface Pt atoms changes in the 5-layer $p(3\times 3)$ Pt(111) slab. | 76 |
| Table 5.1 | Low coverage DFT-revPBE CO adsorption energy, O adsorption energy, CO stretch frequency as the charge of the surface Pt atoms changes. The variation in the surface charge results from changes in the number of electrons in the 5-layer $p(3\times 3)$ Pt(111) slab. | 88 |
| Table 5.2 | High coverage DFT-revPBE CO adsorption energy as the charge of the surface Pt atoms changes. | 90 |
| Table 6.1 | Low coverage DFT-revPBE-vdW-DF di- σ ethylene adsorption energy as the charge of the surface Pt atoms changes. The variation in the surface charge results from changes in the number of electrons in the 5-layer $p(3\times 3)$ Pt(111) slab. | 98 |

List of figures

- Figure 1.1 Structural models of CO adsorption on Co(0001); the large, open circles indicate the close-packed cobalt surface atoms, the small, filled circles indicate the adsorbed CO molecules, and the unit cells are indicated by solid lines. (a) $(\sqrt{3}\times\sqrt{3})R30^\circ$ structure, $\theta=1/3$ ML; (b) $(2\sqrt{3}\times 2\sqrt{3})R30^\circ$ structure, $\theta=7/12$ ML. 4
- Figure 1.2 Illustration of CO-metal bonding at the top site using the frontier-orbital picture, with donation from the CO 5σ orbital to empty metal d-states and backdonation from the metal states to the empty CO- $2\pi^*$ orbitals. 6
- Figure 1.3 Illustration of the orbital interaction of CO with a surface metal atom following the Blyholder model. Only interactions of the 5σ and $2\pi^*$ orbitals of CO and d_{z^2} and d_{xz} metal orbitals are considered. 7
- Figure 1.4 Orbital resolved electronic density of states (DOS) for the top most clean Pt surface layer and for CO (a) 3 Å above the substrate and adsorbed at the (b) top and (c) hollow sites. For CO, the DOS is shown by thick lines shifted by 1.0 with respect to the abscissa. The Fermi level is located at 0 eV. 10
- Figure 1.5 Variation of the CO oxidation rate as measured by the $m/e = 44$ ion current of the mass spectrometer as a function of (a) the CO partial pressure (P_{CO}) for excess O_2 conditions ($P_{O_2}=1200$ Pa). For excess O_2 conditions, the average reaction order is 1.06 ± 0.14 . 13
- Variation of the CO oxidation rate as measured by the $m/e = 44$ ion current of the mass spectrometer as a function of the O_2 partial pressure (P_{O_2}) for excess CO conditions ($P_{CO}=1200$ Pa). For excess CO conditions, the average O_2 reaction order is 0.81 ± 0.10 , Using these reaction orders, rate coefficients for the different catalyst samples were determined (shown in the legend) for 14

excess CO (k_{CO}) conditions.

- Figure 2.1 a) possible CO adsorption sites on a closed packed fcc (111) catalyst surface and a $p(3 \times 3)$ unit cell: T-Top, B-Bridge, F-Hollow-fcc, H-Hollow-hcp. b) A 5 layers $p(3 \times 3)$ model slab in the z – direction with inter-slab spacing of 15 Å. The top three layers are relaxed while the bottom two layers are constrained at the DFT optimized bulk positions. 24
- Figure 2.2 Six vibrational modes are obtained for a adsorbed CO molecule. C-O stretching (1), Co-C stretching (1), frustrated rotation (2) and frustrated translation (2). 26
- Figure 2.3 Natural Bond Orbitals for CO adsorption on Pd (111). (A) Pd-C σ bond (B) C-O σ bond (C) C-O π bond (D) Pd lone pair and C-O π^* bond. 30
- Figure 3.1 Structural models of CO adsorption on Co(0001); the large, open circles indicate the close-packed cobalt surface atoms, the small, filled circles indicate the adsorbed CO molecules, and the unit cells are indicated by solid lines. (a) $(\sqrt{3} \times \sqrt{3})R30^\circ$ structure, $\theta=1/3$ ML; (b) $(2\sqrt{3} \times 2\sqrt{3})R30^\circ$ structure, $\theta=7/12$ ML. 34
- Figure 3.2 Series of PM-RAIR spectra taken on an annealed Co(0001) surface at room temperature at subsequently higher CO pressures from UHV (10 langmuirs of CO dose) to 300 mbar. Intensity and peak position of the signal of linearly bound CO change continuously with pressure. Above 10^{-3} mbar of CO, species attached to bridged sites develop. 35
- Figure 3.3 Differential heat of CO adsorption at 313 K on 20 wt% Co, with different average cobalt particles sizes. 35
- Figure 3.4 Lewis structure resulting from the NBO analysis for CO adsorbed at a top site and CO at a bridge site on Co(0001). 39
- Figure 3.5 Co-C anti-bonding NBO and C-O $2\pi^*$ NBO for CO adsorbed at a top site, $1/3$ ML. 40
- Figure 3.6 Change in the Co(0001) surface Bader charges after CO adsorption at the central Co atom of a $p(3 \times 3)$ unit cell. 43

The central Co atom (orange) loses 0.17 electrons, while the adsorbed CO gains 0.26 electrons. Co atoms along the long diagonal (yellow) lose 0.02 electrons while the Co atoms surrounding the adsorption site remain unchanged. The reduced electron density at the diagonal Co atoms reduces Pauli repulsion with the CO LP NBO and reduces backdonation to the $2\pi^*$ CO orbitals (Table 3.2). The reduced Pauli repulsion in turn strengthens the adsorption at those sites (Table 3.1)

- Figure 3.7 Gibbs free energy of CO adsorption per Co(0001) surface area (kJ/mol Co surface atoms) as a function of pressure at 300 K and 500 K for the various structures in Table 3.1. Only two stable phases are found: a low coverage $(\sqrt{3}\times\sqrt{3})R30^\circ$ -CO phase and a high coverage $(2\sqrt{3}\times 2\sqrt{3})R30^\circ$ -7CO phase. All other structures have a significantly higher ΔG_{ad} . 46
- Figure 3.8 First principle phase diagram for CO adsorption on Co(0001). The two stable phases (Figure 3.1) are separated by a first-order phase transition (line). Both structures are shown and the CO adsorption enthalpies and Gibbs free energies are summarized in Table 3.1. Both structures have been observed experimentally and the conditions where each structure was observed are indicated. (◆) $(\sqrt{3}\times\sqrt{3})R30^\circ$ -CO structure at 7×10^{-9} mbar and 300 K (Bridge et al. [1]). (Δ) $(\sqrt{3}\times\sqrt{3})R30^\circ$ -CO structure below 1 mbar and at 300 K (Beitel et al. [4]). (▲) $(\sqrt{3}\times\sqrt{3})R30^\circ$ -CO structure at 100 mbar and 490 K (Beitel et al. [5]). (●) $(2\sqrt{3}\times 2\sqrt{3})R30^\circ$ -7CO structure at 100 mbar and 300 K (Beitel et al. [5]). (■) Typical FT synthesis conditions: 6 bar and 500 K[15]. 49
- Figure 4.1 Potential energy surface for diffusion from the top to the bridge site. ΔE is the energy difference between the two sites, E_{tb} and E_{bt} are activation energies for site exchange and r_{bt} , r_{tb} the site exchange rates. 55
- Figure 4.2 CO coverage on Pt(111) vs. exposure at $T=200$ K for different pressures 2.0×10^{-9} , 5.3×10^{-8} , 1.0×10^{-7} , 2.4×10^{-7} mbar. Blue symbols: top, open green symbols: bridge, red symbols: total coverage. 56
- Figure 4.3 Schematic representation of the $(\sqrt{3}\times\sqrt{3})R30^\circ$ structure with CO adsorption at top sites on Pt(111). 58

| | | |
|------------|--|----|
| Figure 4.4 | Schematic representation of the $c(4 \times 2)$ -2CO structural model: 1) top view b) side view. | 59 |
| Figure 4.5 | Models proposed for the $c(\sqrt{3} \times 5)$ rect-6CO structure which corresponds to 0.6 ML. (a) Persson et al. (b) Avery et al. (c) Petrova and Yakovkin et al. | 61 |
| Figure 4.6 | Change in the Pt(111)- $p(3 \times 3)$ surface Bader charges after CO adsorption at the central Pt atom of a $p(3 \times 3)$ unit cell. The central Pt atom (orange) loses 0.19 electrons, while the adsorbed CO gains 0.20 electrons. Charge on the Pt atoms surrounding the adsorption site (blue) and along the diagonal (yellow) remain unchanged, hence adsorption of the next CO on the yellow Pt atom is slightly weaker due to through space repulsion (Tables 4.1 and 4.2). | 64 |
| Figure 4.7 | Gibbs free energy of CO adsorption per Pt(111) surface area (kJ/mol Pt surface atoms) as a function of pressure at 300 K for the various structures discussed on section 4.2.1 and 4.2.2. | 70 |
| Figure 4.8 | (a) CO adsorption energies for top and bridge sites at 1/10 ML coverage (b) Differential CO adsorption energies for top and bridge sites at 2/10 ML coverage. Differential adsorption energies are calculated as follows, $\text{Pt}(111)-(\sqrt{3} \times 5)\text{rect}-1\text{CO} + \text{CO}(\text{g}) \rightleftharpoons \text{Pt}(111)-(\sqrt{3} \times 5)\text{rect}-2\text{CO}$. | 72 |
| Figure 4.9 | Change in the Pt(111)- $(\sqrt{3} \times 5)$ rect surface Bader charges (red: charge difference compared to neutral slab, blue: absolute valence charge) before CO adsorption (orange: the Pt atoms which CO binds) and adsorption energies (in green) are shown. (a) low coverage CO adsorption: the charge on the surface Pt atoms is slightly negative (0.05 excess electrons), as expected. (b) High coverage CO adsorption: the Pt atom, which constitutes the top site gain (0.01 excess electron) while the Pt atoms which constitute the bridge site remains unchanged compared to the clean slab charge. Differential adsorption energies are calculated as follows, $\text{Pt}(111)-(\sqrt{3} \times 5)\text{rect}-5\text{CO} + \text{CO}(\text{g}) \rightleftharpoons \text{Pt}(111)-(\sqrt{3} \times 5)\text{rect}-6\text{CO}$. | 74 |

| | | |
|-------------|--|----|
| Figure 4.10 | DFT-revPBE-vdW-DF CO adsorption energy, (■) bridge site (○) top site for 1/9 ML CO on Pt(111) as a function of the charge of the surface Pt atoms. The variation in the surface charge results from changes in the number of electrons in the 5-layer $p(3 \times 3)$ Pt(111) slab. | 77 |
| Figure 5.1 | Arrhenius plot of the CO oxidation rate under excess O ₂ (1200 Pa) and limiting CO (10 Pa) conditions for reaction temperatures of 560, 590 and 615 K. | 83 |
| Figure 5.2 | Effect of the anatase TiO ₂ carrier concentration (N _d) on the CO oxidation rate coefficients for excess CO conditions (k _{CO} , ▲), and for excess O ₂ conditions (k _{O₂} , ■). | 84 |
| Figure 5.3 | a) DFT-revPBE CO adsorption energy (■) and C-O stretch frequency (▲) for 1/9 ML CO at the top side of Pt(111) as a function of the charge of the surface Pt atoms. The variation in the surface charge results from changes in the number of electrons in the 5-layer $p(3 \times 3)$ Pt(111) slab. The neutral slab is indicated by a dotted line and corresponds with a surface charge of 0.05 electrons/Pt atom. | 88 |
| Figure 5.4 | NBO analysis of the effect of charge injection on the calculated CO adsorption energy. Changes in the occupancy of the anti-bonding Pt-C NBO (■) and the C-O 2π* NBO (▲) are shown. The variation in the surface charge results from changes in the number of electrons in the 5-layer $p(3 \times 3)$ Pt(111) slab. The neutral slab is indicated by a dotted line and corresponds with a surface charge of 0.05 electrons/Pt atom. | 91 |
| Figure 6.1 | Schematic of a di adsorption mode of ethylene. | 98 |

Symbols and Abbreviations

Symbols

| | |
|--------------------|--|
| E_{total} | Total electronic energy |
| E_{slab} | Electronic energy of a clean slab |
| $E_{\text{CO(g)}}$ | electronic energy of a gas phase CO molecule |
| T | Temperature |
| P | Pressure |
| G | Gibbs free energy |
| H | Enthalpy |
| S | Entropy |
| h | Planck's constant |
| k | Boltzmann constant |
| R | Gas constant |
| ν_i | Vibrational frequencies of adsorbed species |

Abbreviations

| | |
|----------|---|
| FT | Fischer Tropsch Synthesis |
| TPD | Temperature Programmed Desorption |
| TDS | Thermal Desorption Spectroscopy |
| LEED | Low Energy Electron Diffraction |
| HREELS | High-Resolution Electron Energy Loss Spectroscopy |
| PM-RAIRS | Polarization Modulation Reflection-Absorption Infrared Spectroscopy |
| SSITKA | Steady State Isotopic Transient Kinetic Analysis |
| XPS | X-ray Photoelectron Spectroscopy |
| STM | Scanning Tunnelling Microscopy |
| SMSI | Strong Metal Support Interaction |
| MEIRAS | Multilayer Enhanced Infrared Reflection Absorption Spectroscopy |
| ALD | Atomic Layer Deposition |
| DFT | Density Functional Theory |
| LDA | Local Density Approximation |
| GGA | Generalized Gradient Approximation |
| PBE | Perdew-Burke-Ernzerhof functional |
| revPBE | Revised-Perdew-Burke-Ernzerhof functional |
| PAW | Projector-Augmented-Wave |
| VASP | Vienna Ab-Initio Simulation Package |
| NBO | Natural Bond Orbitals |
| ZPE | Zero-Point Energy |

Publications

1. Y.P. Gavin Chua*, **G.T. Kasun Kalhara Gunasooriya***, Mark Saeys, Edmund G. Seebauer, "Controlling the CO oxidation rate over Pt/TiO₂ catalysts by defect engineering of the TiO₂ support" *Journal of Catalysis* 311 (2014), 306–313.(*Authors contributed equally)
2. **G.T. Kasun Kalhara Gunasooriya**, Mark Saeys, "CO adsorption on Cobalt: first principle prediction of a first order phase transition" (in preparation)
3. **G.T. Kasun Kalhara Gunasooriya**, Mark Saeys, "CO adsorption on Platinum: accurate prediction of site preference and understanding the change in site preference at high coverage" (in preparation)

Chapter 1

Introduction

Carbon monoxide (CO) adsorption and oxidation over transition metal catalysts are arguably the most widely studied catalytic reactions. Due to its simplicity, CO is generally used as a probe molecule in surface science. In this chapter, a general overview of experimental and theoretical studies of CO adsorption on transition metals is presented. Readers are referred to introduction in Chapter 3 and 4 for more specific literature pertinent to CO adsorption on Co and Pt respectively. Next, the electronic nature of the interaction of CO with transition metals surface is explained. Finally, the Schwab effect is introduced and the experimental results demonstrating a gradual variation in the CO oxidation rate over sub-1 nm Pt clusters with the carrier density of the TiO₂ support are presented.

1.1 CO adsorption on transition metal surfaces

The adsorption and reaction of CO on transition metal surfaces has been studied extensively, both experimentally and theoretically, and various well-ordered surface structures have been reported for single crystal surfaces.

1.1.1 Experimental studies

The adsorption of CO on transition metal surfaces has been studied with a variety of experimental techniques [1]. Temperature programmed desorption (TPD), thermal desorption spectroscopy (TDS), work function measurements, low energy electron diffraction (LEED), photoemission spectroscopy, high-resolution electron energy loss spectroscopy (HREELS), and polarization modulation reflection-absorption infrared spectroscopy (PM-RAIRS) are some of the experimental techniques that have been used to characterize CO adsorption on metal surfaces.

Experimentally it is easy to make accurate vibrational measurements for CO/metal systems due to the high dynamic dipole moment of CO, which gives the internal stretching mode a very high intensity both in reflection-absorption infrared spectroscopy (RAIRS) and in high resolution electron energy loss spectroscopy (HREELS) experiments. The frequency of this vibrational mode is primarily dependent on adsorption site and less dependent on the metal on which CO adsorbs. The following general correlations exist: 2000–2100 cm^{-1} indicates atop adsorption, 1850–1950 cm^{-1} indicates bridge adsorption and 1750–1800 cm^{-1} corresponds to threefold hollow adsorption [2, 3]. Hence the experimental determination of the most stable CO adsorption site or sites is

straightforward via vibrational techniques. Other techniques such as X-ray photoelectron spectroscopy also allow for accurate adsorption site determination. XPS is inherently quantitative, as it analyzes the core levels, whose binding energies are element-specific, and sensitive to the binding site, but whose intensities are not influenced by chemical bonding. At the same time, differences of up to several eV in the binding energy of a specific element, the so-called “chemical shifts” allow identifying its local chemical environment and electronic structure [4].

At low coverages, an ordered $(\sqrt{3}\times\sqrt{3})R30^\circ$ -CO structure has been observed using LEED on the (0001) facets of Co [5] and Ru [6] and on the (111) facets of Pt [7], Ni [8], Pd [9], Rh [10] and Ir [11]. At low coverage, CO adsorbs at the top sites on most transition metal surfaces, except on Ni(111) [4] and on Pd(111) [5], where CO also binds at bridge and hollow sites, respectively. For higher coverages, a $(2\sqrt{3}\times 2\sqrt{3})R30^\circ$ -7CO structure, where CO binds at top and bridge site, has been observed on Co(0001) [12], Ru(0001) [13] and Ir(111) [11]. Other ordered structures have been reported as well, e.g., on Pt(111) (4×2) -4CO or $(\sqrt{3}\times 2)$ rect-2CO, $(\sqrt{3}\times 5)$ rect-6CO, $(\sqrt{3}\times 3)$ rect-4CO corresponding to 0.5, 0.6, 0.67 ML, respectively have been reported. [14, 15] The observation of only a limited number of ordered structures rather than a gradual and random build-up of the coverage until saturation, is remarkable, and suggests that the CO adsorption energy has local minima for specific structures as a function of coverage.

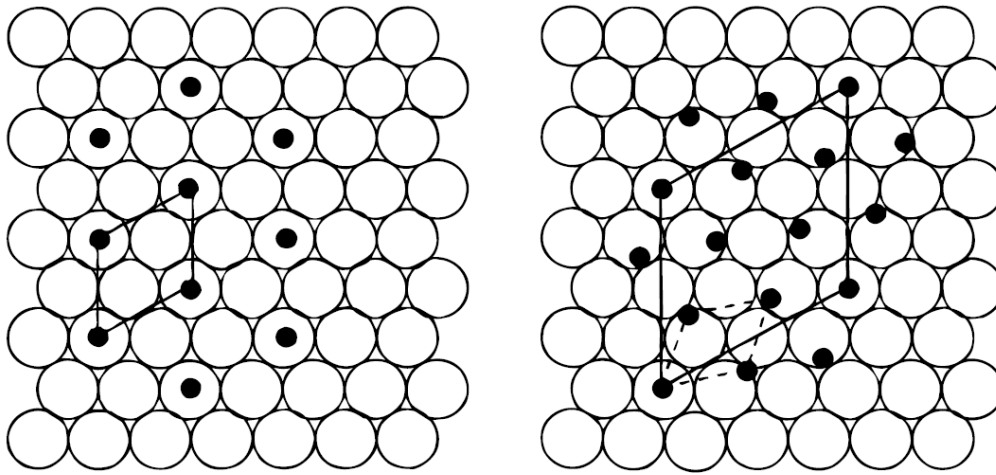


Figure 1.1 Structural models of CO adsorption on Co(0001); the large, open circles indicate the close-packed cobalt surface atoms, the small, filled circles indicate the adsorbed CO molecules, and the unit cells are indicated by solid lines. (a) $(\sqrt{3} \times \sqrt{3})R30^\circ$ structure, $\theta=1/3$ ML; (b) $(2\sqrt{3} \times 2\sqrt{3})R30^\circ$ structure, $\theta=7/12$ ML. Adapted from [16].

1.1.2 Theoretical studies

Theoretically, many studies [17-19] have shown that density functional theory (DFT) using non-hybrid and local functionals such as the Local Density Approximation (LDA) and the Generalized Gradient Approximation (GGA) typically overestimate the CO adsorption energy on transition metal surfaces, and favour hollow sites over top sites, in contradiction with experimental data. This feature has been coined the "CO puzzle" [17]. The overbinding and the incorrect site preference have been attributed to the too small CO 5σ - $2\pi^*$ HOMO-LUMO gap predicted by DFT with those functionals, leading to an overestimation of the backdonation to the $2\pi^*$ LUMO. The CO adsorption model will be discussed in more detail in section 1.1.3. Using the hybrid functional B3LYP, Doll et al. [20] were able to predict the correct adsorption site, indicating that the major part of the error stems from inadequacies in non-hybrid DFT methods in describing the CO-metal interaction. However, B3LYP DFT was recently shown to provide a poor description of metal-metal bonding in the bulk [21].

It was shown by Mason et al. [22] that it is possible to correct for the overbinding of CO primarily at high-coordination sites using the singlet-triplet excitation energy. They further proposed a simple remedy based on the vibrational frequency of the internal CO stretch mode to correct for the overbinding. However, the prediction of the correct site preference and of accurate CO adsorption energies remain important challenges for DFT.

1.1.3 Bonding of CO on transition metal surfaces

The electronic structure provides deep insight into the interaction between adsorbate and surface. There are many papers which deal with electronic structures and their influence on the trends in binding energy or geometrical structure of the CO molecule on metallic surface [23, 24]. The importance of the interplay between the geometric and the electronic structure in the understanding of CO adsorption was stressed by Föhlisch et al. [25].

How does CO adsorb on transition metals? It is generally assumed that a major part of the variation in the CO-metal interaction can be explained in terms of the interaction of the CO frontier molecular orbitals (the highest occupied molecular orbital (HOMO) and the lowest occupied molecular orbital (LUMO) orbitals) with the transition metal d-states. The Blyholder model [26] (illustrated in Figure 1.2) is based on the donation from the occupied CO-5 σ molecular orbital to empty metal surface and back-donation from occupied metal surface states to the empty CO-2 π^* orbitals.

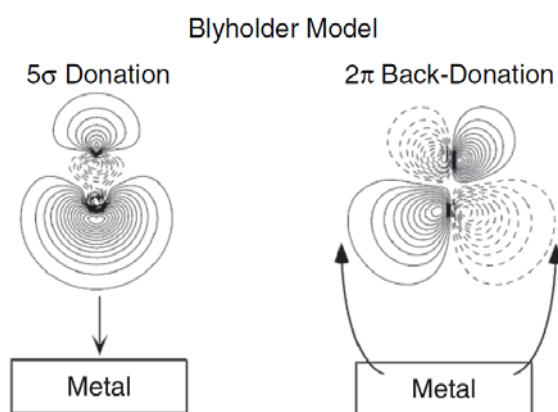


Figure 1.2 Illustration of CO-metal bonding at the top site using the frontier-orbital picture, with donation from the CO 5 σ orbital to empty metal d-states and backdonation from the metal states to the empty CO-2 π^* orbitals. Adapted from [27].

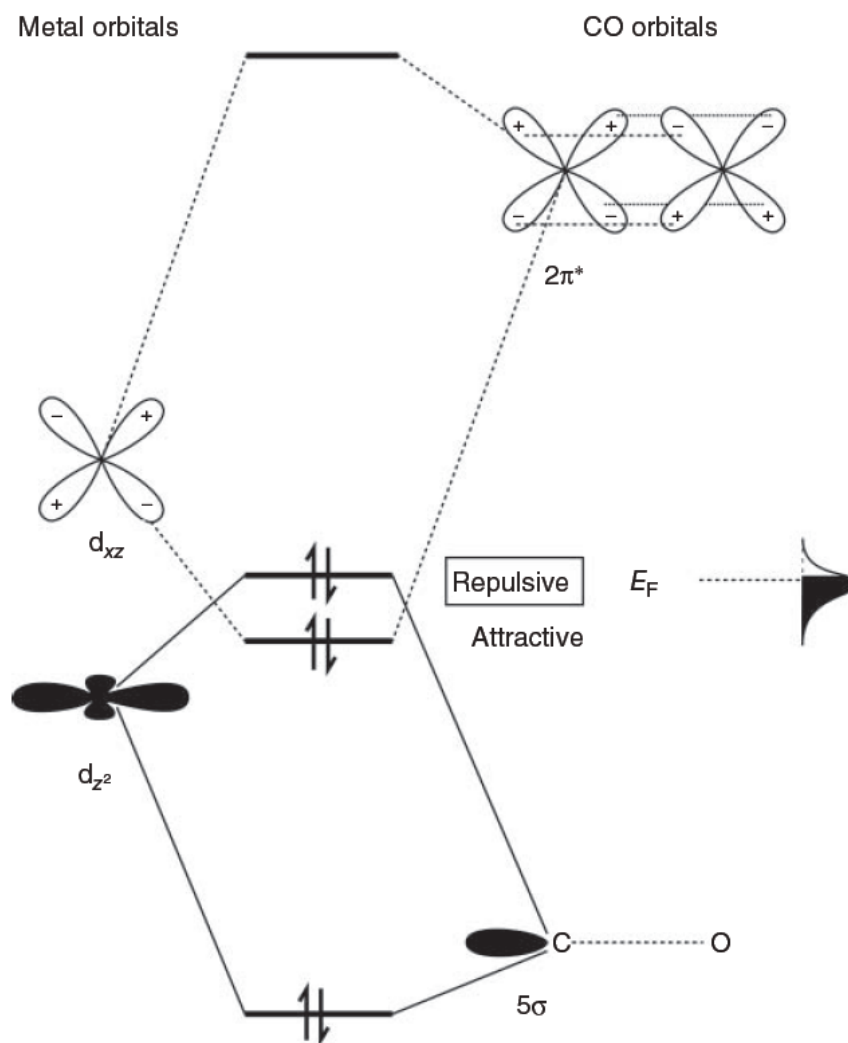


Figure 1.3 Illustration of the orbital interaction of CO with a surface metal atom following the Blyholder model. Only interactions of the 5σ and $2\pi^*$ orbitals of CO and d_{z^2} and d_{xz} metal orbitals are considered. Adapted from [28].

At this point we can divide the literature into four groups. The first group supports the Blyholder model completely [26, 29, 30]. The second group consider the Blyholder model a first approximation, but proposes to include contribution from the 4σ and 1π orbitals. The third group rejects the Blyholder model and proposes an alternative $2\pi^*$ resonance model (e.g. Gumhalter et al. [31]). Finally some authors claim that there is no back-donation to the $2\pi^*$ orbital [32].

For CO adsorption at the top site, the non bonding 5σ CO HOMO (a lone pair on C) interacts with the d_{z^2} states and shifts to lower energies. The d_{z^2} states broaden significantly (thin broken line, Figure 1.3) and split into a 5σ - d_{z^2} bonding contribution well below the Fermi level and completely filled and a 5σ - d_{z^2} antibonding contribution located around the Fermi level. Since two almost fully occupied orbitals interact, the interaction would be only a Pauli-like repulsion (Figure 1.3 & 1.4), if the Pt-CO antibonding 5σ - d_{z^2} states were not pushed partly above the Fermi level and electrons from that state move to anti-bonding M-M states [30]. The depletion of 5σ states is in accordance with the common picture that the 5σ orbital donates electrons to the substrate [26]. The 1π orbital and the $2\pi^*$ CO LUMO, on the other hand, interact with metal d_{yz} and d_{xz} states. The interaction is fairly complicated, and leads to three distinctive energy ranges as shown in Figure 1.4.

For CO adsorption at the hollow site, it is first noted that the interaction is similar to the case of CO at the top site, but since three metal atoms interact with the CO molecule, the modifications of the DOS for each individual metal atom are smaller. To qualitatively evaluate the interaction strength, it is useful to concentrate on the DOS of CO. The bonding CO 5σ -metal d orbital is now at higher energies, indicating a weaker interaction with the d states. This also follows from geometrical and symmetry considerations, which indicate that the 5σ orbital interacts now mainly with d_{xy} and $d_{x^2+y^2}$ states (small peak in the thin dotted line in Figure 1.3 (c) at -6.5 eV]. Due to the increased Pt-C distance, the hybridization is weaker than for the direct 5σ - d_{z^2} interaction for atop adsorption. On the other hand, the 1π and $2\pi^*$ orbitals interact

remarkably effectively with the d_{yz} and d_{xz} states as corroborated by the intensive d_π peak. Furthermore it is noted that the antibonding $2\pi^*-d_{yz}/d_{xz}$ hybrid orbital has moved to much higher energies, so that one can conclude that the $2\pi^*-d_{yz}/d_{xz}$ interaction is the dominant one for the CO adsorption at the hollow site (the $2p^*$ contributions below the Fermi level are predominantly CO-metal bonding). This leads to an important conclusion. Both the 5σ metal d and the $2\pi^*$ -metal d interactions are bonding, and donation from the 5σ orbital to the substrate tends to drive the molecule towards the top site, whereas the back-donation from the substrate to the $2\pi^*$ orbital favours the hollow sites.

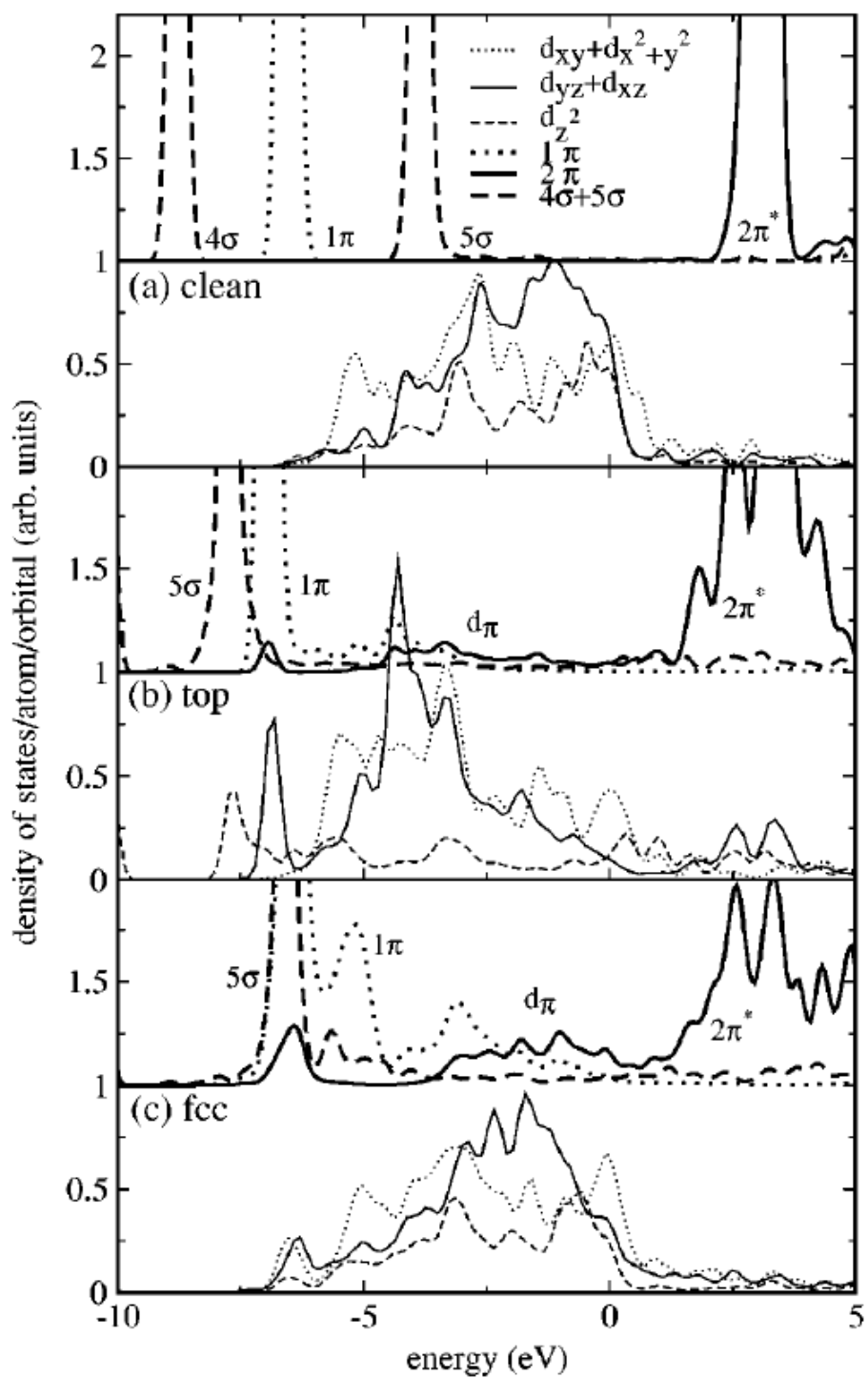


Figure 1.4 Orbital resolved electronic density of states (DOS) for the top most clean Pt surface layer and for CO (a) 3 Å above the substrate and adsorbed at the (b) top and (c) hollow sites. For CO, the DOS is shown by thick lines shifted by 1.0 with respect to the abscissa. The Fermi level is located at 0 eV. Adapted from [19].

1.2 Tuning catalytic activity via the Schwab effect

Since catalysis is a surface phenomenon, precious metal catalyst particles are typically in the nm range to maximize the active surface area. Such nm-sized particles are then dispersed on various types of supports, including metal oxides such as zeolites, titanium dioxide (TiO_2), aluminium oxide (Al_2O_3) and silicon dioxide (SiO_2). The immediate intention of such dispersion is to maximise the surface area in contact with the reactants. Though the supports are often assumed to be inert, it has been found the choice of the support can have an important effect on the catalytic activity, selectivity and stability. A particularly subtle and potentially tuneable effect is the transfer of charge between the metal and the support. As we discussed above, the partial occupancy of the metal-adsorbate orbitals can have an important effect on the metal-adsorbate interaction. Such charge transfer effects are generally known as the Schwab effect.

1.2.1 Schwab effect

The "Schwab effect" [33] refers to the electronic influence that a support exerts on the overlying active catalyst material [33-36]. In principle, this effect provides an opportunity to manipulate catalyst activity and selectivity. Such phenomena were first described in the 1960s [34, 35] and occur either when a metal support influences an overlying metal oxide (Schwab effect of the first type [33]), or when an oxide support influences an overlying metal catalyst (Schwab effect of the second type [33, 36]). In both cases, charge transfer occurs between the metal and the semiconductor, leading to a modification of the catalyst surface charge density and hence its catalytic activity. The Schwab

effect is purely an electronic effect and does not involve the migration of any species, unlike the strong metal support interaction (SMSI) first observed by Tauster and co-workers in the 1970s [37].

The Schwab effect of the second type offers the possibility to control the activity of a supported metal catalyst by manipulating the carrier concentration of the semiconducting oxide support. The potential benefits have attracted several studies into the Schwab effect. For example, when Pt is supported on TiO₂ doped with higher valence cations (Ta⁵⁺, Sb⁵⁺, W⁶⁺), its Fermi energy increases. This decreases the CO chemisorption capacity [38] and decreases the CO oxidation rate [39, 40]. More recently, Deshlera et al. [41] illustrated a Schwab effect of the second type for a Pt/TiO₂ catalytic diode. Using multilayer enhanced infrared reflection absorption spectroscopy (MEIRAS), they demonstrated that the C-O bond of adsorbed CO strengthens (weakens) when an external forward (reverse) bias is applied to the catalytic diode, thereby implying a variation in the Pt-CO bond strength.

Recently, the Saeys group [42, 43] reported a gradual variation in the experimental CO oxidation rate over sub-1 nm Pt clusters when the carrier density of the TiO₂ support is tuned (Schwab effect of the second type).

1.2.2 Tuning the CO oxidation rate over Pt/TiO₂ catalysts by defect engineering of the TiO₂ support

The Saeys group studied CO oxidation over a series of Pt catalysts supported on polycrystalline thin films of anatase TiO₂. The anatase films were synthesized in Seebauer group [44, 45] and show a variation of an order of magnitude in the n-type carrier concentration. The effect of the support carrier concentration on the electronic structure of the small Pt particles supported on the TiO₂ was demonstrated by photoelectron spectroscopy, while the effect on the catalytic activity was measured in a vacuum chamber for both excess CO and excess O₂ conditions. The reaction rate for all four samples is plotted as a function of the partial pressure of the limiting reactant in Figures 1.5 and 1.6.

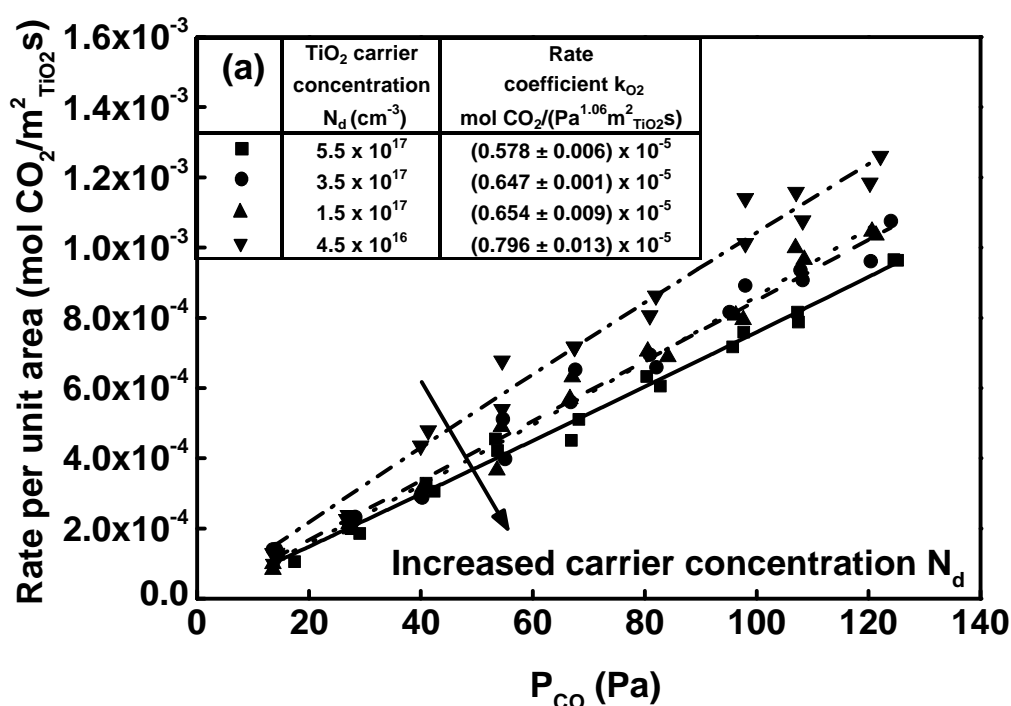


Figure 1.5 Variation of the CO oxidation rate as measured by the $m/e = 44$ ion current of the mass spectrometer as a function of (a) the CO partial pressure (P_{CO}) for excess O₂ conditions ($P_{O_2}=1200$ Pa). For excess O₂ conditions, the average reaction order is 1.06 ± 0.14 . Adapted from [42].

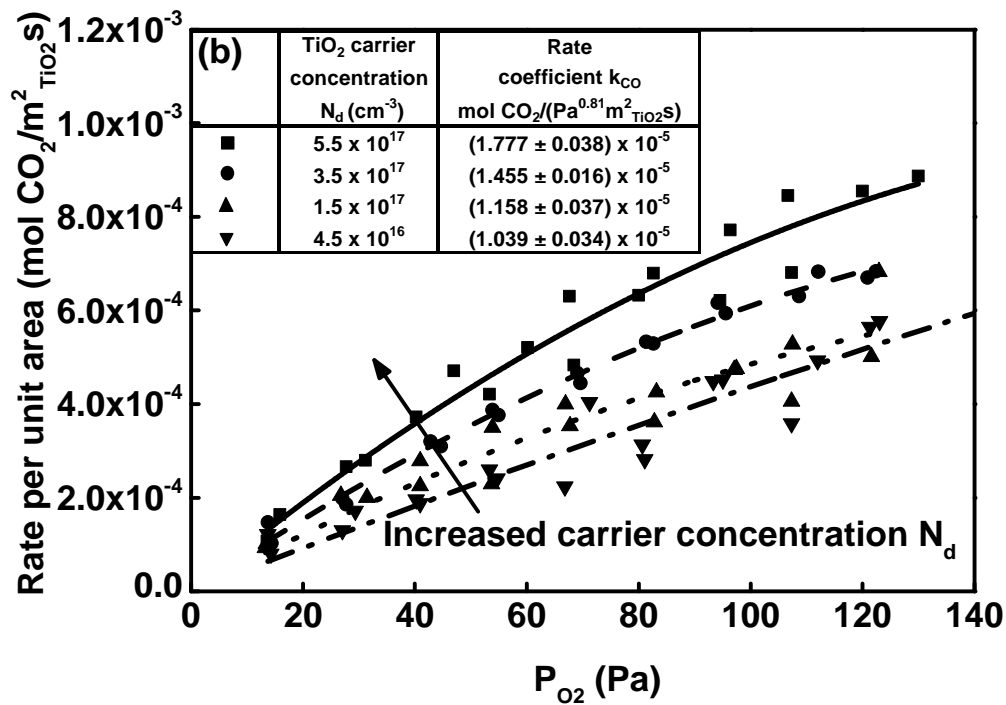


Figure 1.6 Variation of the CO oxidation rate as measured by the $m/e = 44$ ion current of the mass spectrometer as a function of the O_2 partial pressure (P_{O_2}) for excess CO conditions ($P_{CO}=1200$ Pa). For excess CO conditions, the average O_2 reaction order is 0.81 ± 0.10 . Using these reaction orders, rate coefficients for the different catalyst samples were determined (shown in the legend) for excess CO (k_{CO}) conditions. Adapted from [42].

For excess O_2 conditions (Figure 1.5) the reaction rate decreased with increasing carrier concentration, while for excess CO conditions (Figure 1.6) the rate increased with increasing carrier concentration. For excess O_2 conditions, an average CO reaction order of 1.06 ± 0.14 is determined for the four samples, suggesting that CO adsorption is kinetically relevant [24]. For excess CO conditions, the average O_2 reaction order for the four samples is 0.81 ± 0.10 . The effective reaction rate coefficient depends on the carrier concentration.

1.3 Thesis structure

In this thesis the adsorption of carbon monoxide on cobalt and platinum catalysts is studied. Though this is probably one of the most studied systems, several interesting observations are made. The organization of this thesis as follows: Chapter 2 briefly discusses the computational methods, catalysts models and various tools used to analyze the results. In Chapter 3, CO adsorption on Co(0001) terraces is studied. Adsorption of CO is a critical step during Fischer Tropsch Synthesis and typically high coverages are observed under FT conditions. The calculations demonstrate that there are only 2 stable phases on infinite Co terraces, and they are separated by a first order phase transition. The predicted phase transition temperature nicely matches the conditions where the two phases have been observed experimentally. All other phases are significantly less stable. In Chapter 4, CO adsorption on Pt(111) terraces is studied. The situation is much more complex on Pt terraces than on Co terraces with many competing phases which are close in Gibbs free energy. Accurate site prediction and the increase in stability of bridge CO over top CO at high coverage are analyzed in detail. To elucidate these trends, Bader charges and the occupancies of the Natural Bond Orbitals corresponding to a Lewis structure are used. In chapter 5, the effect of charge transfer to Pt on the CO adsorption energy was studied in detail by DFT in order to elucidate the gradual variation in the CO oxidation rate over sub-1 nm Pt clusters when the carrier density of the TiO₂ support is tuned (Schwab effect) as observed previously by the Saeys group [42, 43]. DFT calculations and NBO analysis demonstrate that charge injection into the Pt particles reduces the CO adsorption energy by increasing the Pauli repulsion between the filled CO 5 σ

and Pt d_{z^2} orbitals, explaining the reaction rate trends observed experimentally by Chua [42, 43]. Finally, the thesis concludes with a summary of the main findings and with suggestions for future work.

1.4 References

- [1] G.A. Somorjai, Y. Li, Introduction to Surface Chemistry and Catalysis, Wiley, 2010.
- [2] F.M. Hoffmann, Surf. Sci. Rep., 3 (1983) 107.
- [3] R.J.H. Clark, R.E. Hester, Advances in infrared and Raman spectroscopy, Wiley, New York, 1985.
- [4] C. Papp, H.-P. Steinrück, Surf. Sci. Rep., 68 (2013) 446.
- [5] M.E. Bridge, C.M. Comrie, R.M. Lambert, Surf. Sci., 67 (1977) 393.
- [6] E.D. Williams, W.H. Weinberg, Surf. Sci., 82 (1979) 93.
- [7] G. Ertl, M. Neumann, K.M. Streit, Surf. Sci., 64 (1977) 393.
- [8] K. Christmann, O. Schober, G. Ertl, The Journal of Chemical Physics, 60 (1974) 4719.
- [9] H. Ohtani, M.A.V. Hove, G.A. Somorjai, Surf. Sci., 187 (1987) 372.
- [10] P.A. Thiel, E.D. Williams, J.T. Yates Jr, W.H. Weinberg, Surf. Sci., 84 (1979) 54.
- [11] J. Lauterbach, R.W. Boyle, M. Schick, W.J. Mitchell, B. Meng, W.H. Weinberg, Surf. Sci., 350 (1996) 32.
- [12] H. Papp, Surf. Sci., 129 (1983) 205.
- [13] H. Pfnür, D. Menzel, F.M. Hoffmann, A. Ortega, A.M. Bradshaw, Surf. Sci., 93 (1980) 431.
- [14] J.P. Biberian, M.A. Van Hove, Surf. Sci., 138 (1984) 361.
- [15] G.T.K.K. Gunasooriya, M. Saeys, (2014).
- [16] G.A. Beitel, A. Laskov, H. Oosterbeek, E.W. Kuipers, J Phys Chem-U, 100 (1996) 12494.

- [17] P.J. Feibelman, B. Hammer, J.K. Nørskov, F. Wagner, M. Scheffler, R. Stumpf, R. Watwe, J. Dumesic, *The Journal of Physical Chemistry B*, 105 (2001) 4018.
- [18] A. Gil, A. Clotet, J.M. Ricart, G. Kresse, García, amp, x, M. a-Hernández, N. Rösch, P. Sautet, *Surf. Sci.*, 530 (2003) 71.
- [19] G. Kresse, A. Gil, P. Sautet, *Physical Review B*, 68 (2003) 073401.
- [20] K. Doll, *Surf. Sci.*, 573 (2004) 464.
- [21] A. Roldán, F. Viñes, F. Illas, J. Ricart, K. Neyman, *Theor. Chem. Acc.*, 120 (2008) 565.
- [22] S.E. Mason, I. Grinberg, A.M. Rappe, *Physical Review B*, 69 (2004) 161401.
- [23] B. Hammer, J.K. Nørskov, *Theoretical surface science and catalysis—calculations and concepts*, in: H.K. Bruce C. Gates (Ed.) *Advances in Catalysis*, Academic Press, 2000, pp. 71.
- [24] S.-i. Ishi, Y. Ohno, B. Viswanathan, *Surf. Sci.*, 161 (1985) 349.
- [25] A. Föhlisch, M. Nyberg, J. Hasselström, O. Karis, L.G.M. Pettersson, A. Nilsson, *Phys. Rev. Lett.*, 85 (2000) 3309.
- [26] G. Blyholder, *The Journal of Physical Chemistry*, 68 (1964) 2772.
- [27] A. Nilsson, L.G.M. Pettersson, J.K. Nørskov, *Chemical Bonding at surfaces and interfaces* Elsevier, The Netherlands 2008.
- [28] R.A. van Santen, I.A.W. Filot, *The Quantum Chemistry of Transition Metal Surface Bonding and Reactivity*, in: *The Chemical Bond*, Wiley-VCH Verlag GmbH & Co. KGaA, 2014, pp. 269.
- [29] F. Illas, S. Zurita, A.M. Márquez, J. Rubio, *Surf. Sci.*, 376 (1997) 279.
- [30] H. Aizawa, S. Tsuneyuki, *Surf. Sci.*, 399 (1998) L364.

- [31] B. Gumhalter, K. Wandelt, P. Avouris, *Physical Review B*, 37 (1988) 8048.
- [32] S. Ohnishi, N. Watari, *Physical Review B*, 49 (1994) 14619.
- [33] M. Boudart, G. Djega-Mariadassou, *Kinetics of Heterogeneous Catalytic Reactions*, Princeton University Press, Princeton 1984.
- [34] G.M. Schwab, K. Koller, *J. Am. Chem. Soc.*, 90 (1968) 3078.
- [35] G.M. Schwab, *Surf. Sci.*, 13 (1969) 198.
- [36] R.A. Van Santen, *J. Mol. Catal.*, 54 (1989) 288.
- [37] S.J. Tauster, *Acc. Chem. Res.*, 20 (1987) 389.
- [38] E.C. Akubuiro, X.E. Verykios, *J. Catal.*, 113 (1988) 106.
- [39] E.C. Akubuiro, X.E. Verykios, T. Ioannides, *Applied Catalysis*, 46 (1989) 297.
- [40] E.C. Akubuiro, T. Ioannides, X.E. Verykios, *J. Catal.*, 116 (1989) 590.
- [41] P. Deshlahra, W.F. Schneider, G.H. Bernstein, E.E. Wolf, *J. Am. Chem. Soc.*, 133 (2011) 16459.
- [42] Y.P.G. Chua, PhD Thesis, National University of Singapore, Singapore (2013)
- [43] Y.P.G. Chua, G.T.K.K. Gunasooriya, M. Saeys, E.G. Seebauer, *J. Catal.*, 311 (2014) 306.
- [44] M.C.K. Sellers, E.G. Seebauer, *Thin Solid Films*, 519 (2011) 2103.
- [45] M.C.K. Sellers, E.G. Seebauer, *Journal of Vacuum Science & Technology A: Vacuum, Surfaces, and Films*, 29 (2011) 061503.

Chapter 2

Computational method and models

In this chapter, few quantum chemical calculations that were used in this thesis are briefly introduced, followed by a detailed account of the computational models and tools utilized for the calculations.

2.1 Density Functional Theory

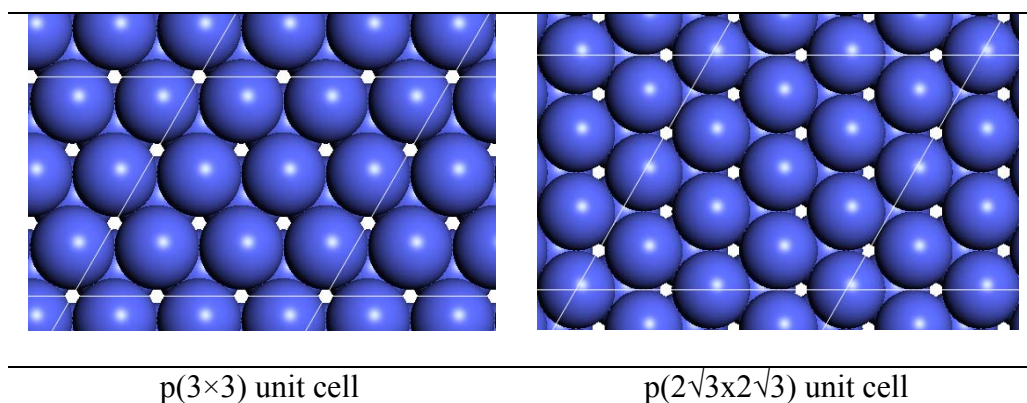
Density Functional Theory (DFT) was developed by Kohn, Hohenberg and Sham [1, 2] and is widely used to obtain approximate solutions to the Schrödinger equation. The rise of DFT and its uptake in academia and industry has been widely discussed, and was perhaps illustrated most clearly in Burke's recent Spotlight article [3]. A detailed technical account of DFT can be found in Parr and Yang [4]. For a shorter introduction, the reader is referred to the Nobel lecture of Walter Kohn [5].

2.2 Catalyst models

2.2.1 Cobalt catalyst models

The Co catalyst was modelled as a five-layer hcp Co(0001) slab, using a $p(3\times 3)$ unit cell with nine surface atoms per layer and using a $(2\sqrt{3}\times 2\sqrt{3})R30^\circ$ unit cell with 12 surface atoms per layer. The bottom two layers were constrained at the bulk positions with an optimized lattice constant of 2.495 Å (the experimental value is 2.51 [6]).

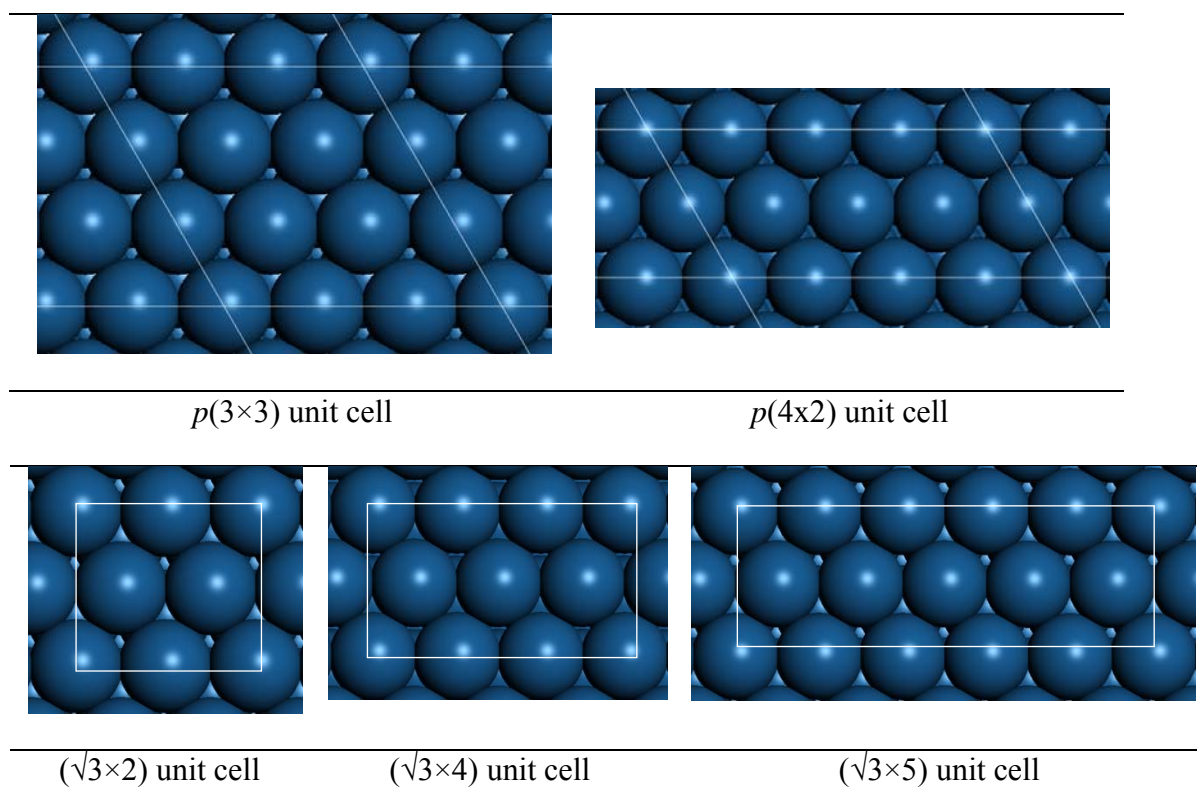
Table 2.1 Top view of the five different unit cells considered in chapter 3 of this thesis; $p(3\times 3)$, $p(2\sqrt{3}\times 2\sqrt{3})$ unit cells.



2.2.2 Platinum catalyst models

The Pt catalyst was modelled as a five layer fcc Pt(111) slab. Five different unit cells were considered; a $p(3\times 3)$ unit cell with nine Pt atoms per layer, a $p(4\times 2)$ unit cell with eight Pt atoms per layer, a $(\sqrt{3}\times 2)$ unit cell with four Pt atoms per layer, a $(\sqrt{3}\times 5)$ unit cell with ten Pt atoms per layer a $(\sqrt{3}\times 3)$ unit cell with six Pt atoms per layer. The bottom two layers were constrained at the bulk positions with an optimized lattice constant of 4.028 Å (the experimental value is 3.920 Å [6]).

Table 2.2 Top view of the five different unit cells considered in the chapter 4 of this thesis; $p(3\times 3)$, $p(4\times 2)$, $(\sqrt{3}\times 2)$, $(\sqrt{3}\times 5)$ and $(\sqrt{3}\times 4)$ unit cells



2.3 VASP calculations

Adsorption energies were calculated using periodic spin-polarized Density Functional Theory (DFT) with the revised Perdew-Burke-Ernzerh of functional (revPBE) [7] and including non-local vdW-DF correlation [8, 9], as implemented in the Vienna Ab-initio Simulation Package (VASP) [10, 11]. A plane-wave basis set with a cut-off kinetic energy of 450 eV, and the electron-ion interactions were described by the projector-augmented wave (PAW) method [12]. The top three layers and the adsorbed CO were fully optimized. An inter-slab spacing of 15 Å was found to minimize interactions between repeated slabs. The number of k-points sample in irreducible part of Brillouin zone is important for the accurate integration of the properties computed in reciprocal space. The k-points mesh was generated following the Monkhorst-Pack [13] procedure. In this study, the Brillouin zone was sampled with a $(3 \times 3 \times 1)$ Monkhorst-Pack grid for $p(3 \times 3)$, $(2\sqrt{3} \times 2\sqrt{3})R30^\circ$ and $p(4 \times 2)$ unit cells and a $(5 \times 3 \times 1)$ Monkhorst-Pack grid for the other unit cells. Geometries were optimized until the energy between consecutive steps changes by less than 0.1 kJ/mol.

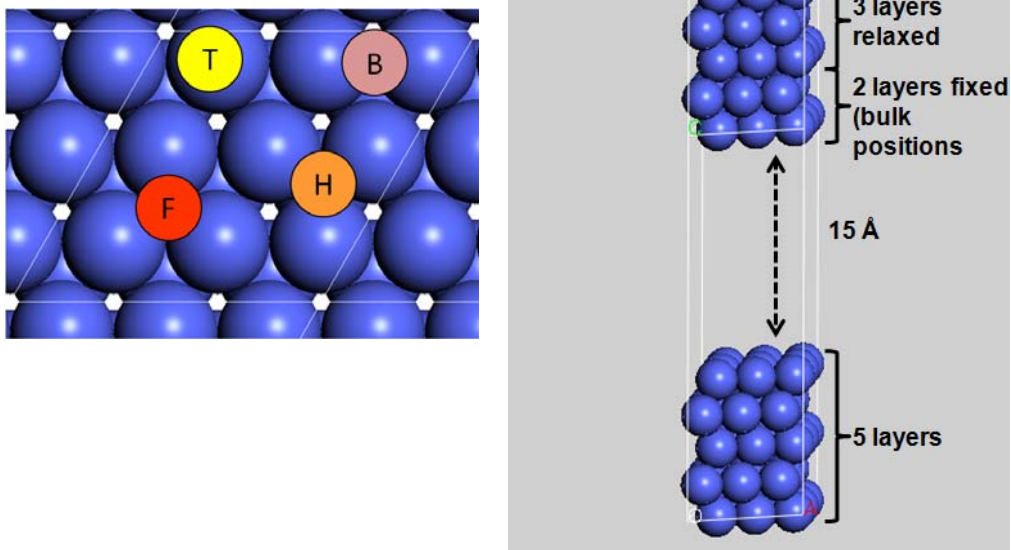


Figure 2.1 a) possible CO adsorption sites on a closed packed fcc (111) catalyst surface and a p(3x3) unit cell: T-Top, B-Bridge, F-Hollow-fcc, H-Hollow-hcp. b) A 5 layers p(3x3) model slab in the z – direction with inter-slab spacing of 15 Å. The top three layers are relaxed while the bottom two layers are constrained at the DFT optimized bulk positions.

2.3.1 Adsorption energy

CO adsorption energies are calculated as follows;

$$\text{Average } E_{\text{adsorption of CO}} = \frac{E_{\text{total}} - E_{\text{slab}} - nE_{\text{CO(g)}}}{n} \quad (2.1)$$

Where, E_{total} , E_{slab} and $E_{\text{CO(g)}}$ are the electronic energies of CO on a model slab, clean model slab and CO molecule in gas phase without any interactions respectively, n is the number of CO molecules per unit cell.

Example 1

A sample adsorption energy calculation for the adsorption of a single and 3 CO molecules at the top sites of a Co(0001) p(3x3) surface is shown below.

| | | |
|-------------------------|---------|---------|
| E_{total} (eV) | -163.90 | -189.51 |
| E_{slab} (eV) | -151.17 | -151.17 |
| $E_{\text{CO(g)}}$ (eV) | -11.38 | -11.38 |
| n | 1 | 3 |

Using equation 2.1 yields, $E_{\text{adsorption CO}} = -1.35$ eV ($n=1$), -1.40 eV ($n=3$)

1 eV per CO molecule is equivalent to 96.485 kJ/mol,

hence, $E_{\text{adsorption CO}} = -130.0$ kJ/mol ($n=1$), -134.9 kJ/mol ($n=3$)

2.3.2 Gibbs Free energy

To evaluate the thermodynamic stability of the adsorbed CO as a function of pressure and temperature, Gibbs free energies of adsorption, $\Delta G_{\text{ads}}(T, p)$, were calculated with reference to a gas phase reservoir of CO. The equation for the Gibbs free energy (ΔG) is given as follows,

$$\Delta G_{\text{ads}}(T, p) = \Delta H(T) - T\Delta S + RT \ln \left(\frac{1}{P_{\text{CO}}} \right) \quad (2.2)$$

The VASP electronic energies corresponds to $T = 0$ K and $p = 0$ Pa. In order to calculate the Gibbs free energies zero-point energies (ZPE), enthalpy (H) temperature corrections, and entropies (S) are required. They were computed using the harmonic oscillator approximation [14]. First, the vibrational frequencies of adsorbed species were therefore calculated.

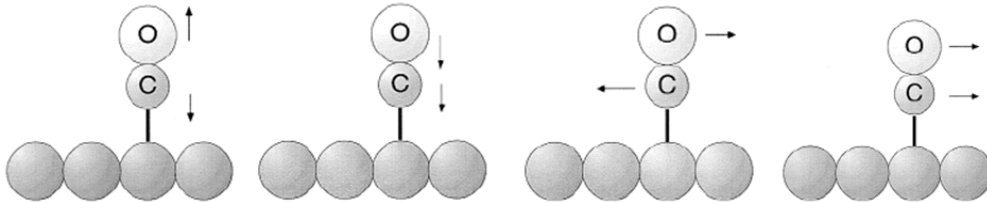


Figure 2.2 Six vibrational modes are obtained for a adsorbed CO molecule. C-O stretching (1), Co-C stretching (1), frustrated rotation (2) and frustrated translation (2). Adopted from [14].

Next, the zero-point energies (Equation 2.3), enthalpy corrections (Equation 2.4) and entropies (Equation 2.5) are computed using vibrational partition functions.

$$\text{ZPE} = \frac{1}{2} \sum_{i=1}^n h\nu_i \quad (2.3)$$

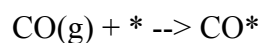
$$[\text{H(T)} - \text{H(0)}]_{\text{vib}} = \text{RT} \sum_i \left(\frac{h\nu_i}{\text{kT}} \right) \frac{e^{-\frac{h\nu_i}{\text{kT}}}}{\left(1 - e^{-\frac{h\nu_i}{\text{kT}}} \right)} \quad (2.4)$$

$$\text{S}_{\text{vib}} = -\text{R} \sum_i \ln \left(1 - e^{-\frac{h\nu_i}{\text{kT}}} \right) + \text{R} \sum_i \left(\frac{h\nu_i}{\text{kT}} \right) \frac{e^{-\frac{h\nu_i}{\text{kT}}}}{\left(1 - e^{-\frac{h\nu_i}{\text{kT}}} \right)} \quad (2.5)$$

Where, $h = 6.626 \times 10^{-34}$ J.s is the Planck's constant, ν_i - vibrational frequencies of adsorbed species in s^{-1} , $\text{R} = 8.314$ J/mol.K is the gas constant, $k = 1.381 \times 10^{-23}$ J/K is the Boltzmann constant.

Example 2

A sample Gibbs free adsorption energy calculation for the adsorption of a single CO molecule at the top site of a Co(0001) p(3x3) surface is shown below.



| | CO(g) | CO* (top site) |
|--|-------|----------------|
| Zero-point energies (kJ/mol) | 12.7 | 19.0 |
| $\Delta H_{\text{correction to 300 K}}$ (kJ/mol) | 8.7 | 7.1 |
| S at 300 K (J/mol K) | 197.8 | 54.3 |
| Partial Pressure (bar) | 0.001 | - |

$$\Delta H (300 \text{ K}) = -130.0(\text{from Example 1}) + (19-12.7) + (7.1-8.7) = -125.2 \text{ kJ/mol}$$

$$\Delta S = (54.3 - 197.8) = -143.5 \text{ J/mol K}$$

$$\begin{aligned} \Delta G (300\text{K}, 1\text{mbar}) &= -125.2 - (300/1000)(-143.5) + 8.3(300/1000)\ln(1/0.001) \\ &= -64.9 \text{ kJ/mol} \end{aligned}$$

Above example shows how to obtain Gibbs free energies and include the effects of temperature and pressure.

2.3.3 Bader Charge

Atomic charges in molecules or in solids are not observable quantities in quantum mechanics. Many different schemes have therefore been proposed to partition the electron density and assign charges to individual atoms in a molecule to underpin our chemical intuition. Schemes such as, Mulliken populations analysis, density matrix based normal populations analysis are based on electronic orbitals while Bader analysis and Hirshfeld analysis are based on charge density.

The Bader charge method uses zero flux surfaces to divide atoms. A zero flux surface is a 2-D surface on which the charge density is minimum. Typically in molecular systems, the charge density reaches a minimum between atoms and this is a natural place to separate region of influence of the different atoms similar to the concept of water management. In this thesis, Bader charges were computed to quantify the effect of charge transfer on bonding [15].

2.3.4 Natural Bond Orbitals

Natural Bond Orbital (NBO) analysis [16, 17] has been successfully applied to understand chemical bonding in molecules [18, 19]. NBOs consist of a set of orthonormal localized “maximum occupancy” orbitals that give a Lewis-type description of the total electron density. The Lewis-type NBOs (2-center bonds, valence lone pairs and one-center core orbitals) along with the “non-Lewis”-type NBOs (valence anti-bonding orbitals, nonbonding orbitals and Rydberg states) describe the localized Lewis representation of the wavefunction and the residual "delocalization effects" (i.e., departures from a

single, localized Lewis structure) respectively. Thus, NBOs provide a valence bond-type description of the wavefunction, closely linked to classical Lewis structure concepts. This localized picture of the orbitals is very useful to understand systems in which the electrons are strongly correlated.

The NBO algorithm has recently been implemented for periodic calculations [20] and can now be used to analyze metal-adsorbate interactions. In this thesis, the bonding of CO on Co(0001) and Pt(111) were analyzed using the Natural Bond Orbitals and visualized using Visual Molecular Dynamics software (VMD 1.9.1)

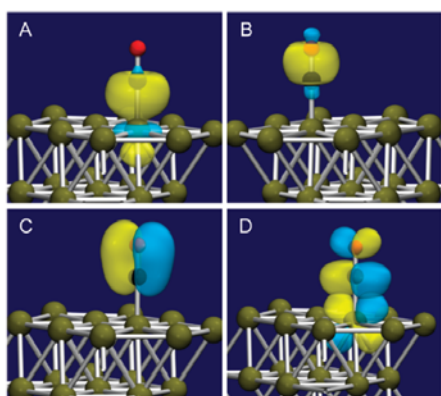


Figure 2. NBOs of CO adsorption on Pd(111). (A) Pd-C σ bond; (B) C-O σ bond; (C) C-O π bond; (D) Pd lone pair and C-O π^* bond.

Table 4. NBOs of CO adsorption of Pd(111)

| NBO | occupancy | center (bond % contribution) | hybridization (function, %) |
|-----------------|-----------|------------------------------|--------------------------------|
| Pd-C σ | 1.980 | C (53) Pd(47) | s 63, p 37 s 12, p 11, d 78 |
| Pd-C σ^* | 0.524 | C (47) Pd(53) | s 63, p 37 s 12, p 11, d 78 |
| C-O σ | 1.992 | C(31) O(69) | s 38, p 62 s 43, p 57 |
| C-O σ^* | 0.019 | C(69) O(31) | s 38, p 62 s 43, p 57 |
| C-O π | 1.991 | C(28) O(72) | p 100 p 100 |
| C-O π^* | 0.202 | C(72) O(28) | p 100 p 100 |
| Pd d_{z^2} LP | 1.810 | Pd(100) | d 100 |
| Pd d_{yz} LP | 1.810 | Pd(100) | d 100 |

Figure 2.3 Natural Bond Orbitals for CO adsorption on Pd (111). (A) Pd-C σ bond (B) C-O σ bond (C) C-O π bond (D) Pd lone pair and C-O π^* bond. Adopted from [20].

2.4 References

- [1] P. Hohenberg, W. Kohn, *Physical Review*, 136 (1964) B864.
- [2] W. Kohn, L.J. Sham, *Physical Review*, 140 (1965) A1133.
- [3] K. Burke, *The Journal of Chemical Physics*, 136 (2012).
- [4] J.-L. Calais, *Int. J. Quantum Chem*, 47 (1993) 101.
- [5] W. Kohn, *Electronic structure of matter - wave functions and density functionals*, in: *Nobel Lecture*, 1999.
- [6] R.W.G. Wyckoff, *Crystal Structures*, Krieger Publishing, Malabar FL, 1982.
- [7] Y. Zhang, W. Yang, *Phys. Rev. Lett.*, 80 (1998) 890.
- [8] M. Dion, H. Rydberg, E. Schröder, D.C. Langreth, B.I. Lundqvist, *Phys. Rev. Lett.*, 92 (2004) 246401.
- [9] J. Klimeš, D.R. Bowler, A. Michaelides, *Physical Review B*, 83 (2011) 195131.
- [10] G. Kresse, J. Furthmüller, *Computational Materials Science*, 6 (1996) 15.
- [11] G. Kresse, J. Furthmüller, *Physical Review B*, 54 (1996) 11169.
- [12] P.E. Blöchl, *Physical Review B*, 50 (1994) 17953.
- [13] H.J. Monkhorst, J.D. Pack, *Physical Review B*, 13 (1976) 5188.
- [14] I. Chorkendorff, J.W. Niemantsverdriet, *Concepts of Modern Catalysis and Kinetics*, Wiley-VCH, 2007.
- [15] R.F.W. Bader, *Atoms in Molecules - A Quantum Theory*, Oxford University Press, Oxford, 1990.
- [16] J.P. Foster, F. Weinhold, *J. Am. Chem. Soc.*, 102 (1980) 7211.
- [17] F. Weinhold, C. Landis, *Valency and Bonding - A Natural Bond Orbital Donor-Acceptor Perspective*, Cambridge University Press, Cambridge, 2005.

- [18] C.-Y. Sung, L.J. Broadbelt, R.Q. Snurr, *Catal. Today*, 136 (2008) 64.
- [19] S. Wannakao, P. Khongpracha, J. Limtrakul, *The Journal of Physical Chemistry A*, 115 (2011) 12486.
- [20] B.D. Dunnington, J.R. Schmidt, *Journal of Chemical Theory and Computation*, 8 (2012) 1902.

Chapter 3

CO adsorption on Cobalt: first principle prediction of a first order phase transition

3.1 Introduction

The adsorption of CO on Co(0001) has been studied with a wide range of experimental techniques [1-6]. For coverages up to 1/3 ML, an isosteric heat of adsorption of -128 kJ/mol was measured on Co(0001) single crystals [2]. At higher coverages, the heat of adsorption decreases to -96 kJ/mol [2]. On supported Co/ γ -Al₂O₃ catalysts with typical Co particle sizes between 5 and 17 nm, the measured heat of adsorption ranges from -121 to -139 kJ/mol [6]. Low energy electron diffraction (LEED) studies show a $(\sqrt{3}\times\sqrt{3})R30^\circ$ structure (Figure 3.1) with CO at top sites at 100 K and for an exposure of 1.2 L [2], at 160 K and for an exposure of 1.25 L [7] and at 300 K and for a CO pressure of 7×10^{-9} mbar [1]. Polarization modulation reflection-adsorption infrared spectroscopy (PM-RAIRS) [4] shows that the $(\sqrt{3}\times\sqrt{3})R30^\circ$ structure persists for pressures up to 1 mbar at 300 K. For this structure, both PM-RAIRS and

high-resolution electron energy loss spectroscopy (HREELS) find a single IR peak near 2000 cm^{-1} , corresponding to CO at top sites [3, 4]. When the CO exposure is increased to 2.2 L at 100 K, LEED shows a transition to a $(2\sqrt{3}\times 2\sqrt{3})R30^\circ$ structure (Figure 3.1) with one atop CO and six bridge COs per unit cell, corresponding to a coverage of $7/12\text{ ML}$ [2].

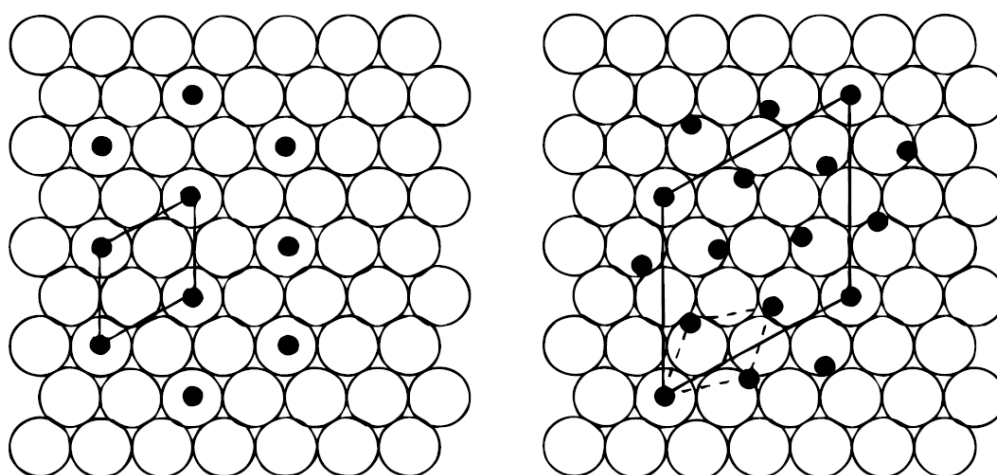


Figure 3.1 Structural models of CO adsorption on Co(0001); the large, open circles indicate the close-packed cobalt surface atoms, the small, filled circles indicate the adsorbed CO molecules, and the unit cells are indicated by solid lines. (a) $(\sqrt{3}\times\sqrt{3})R30^\circ$ structure, $\theta=1/3\text{ ML}$; (b) $(2\sqrt{3}\times 2\sqrt{3})R30^\circ$ structure, $\theta=7/12\text{ ML}$. Adapted from [4].

The $(2\sqrt{3}\times 2\sqrt{3})R30^\circ$ structure was also observed with PM-RAIRS above 1 mbar at 300 K [4]. In the vibrational spectrum, an additional peak at 1850 cm^{-1} is observed, corresponding to bridge CO. When the temperature is subsequently increased to 490 K at 300 mbar, some CO desorbs and the $(\sqrt{3}\times\sqrt{3})R30^\circ$ structure re-emerges [5].

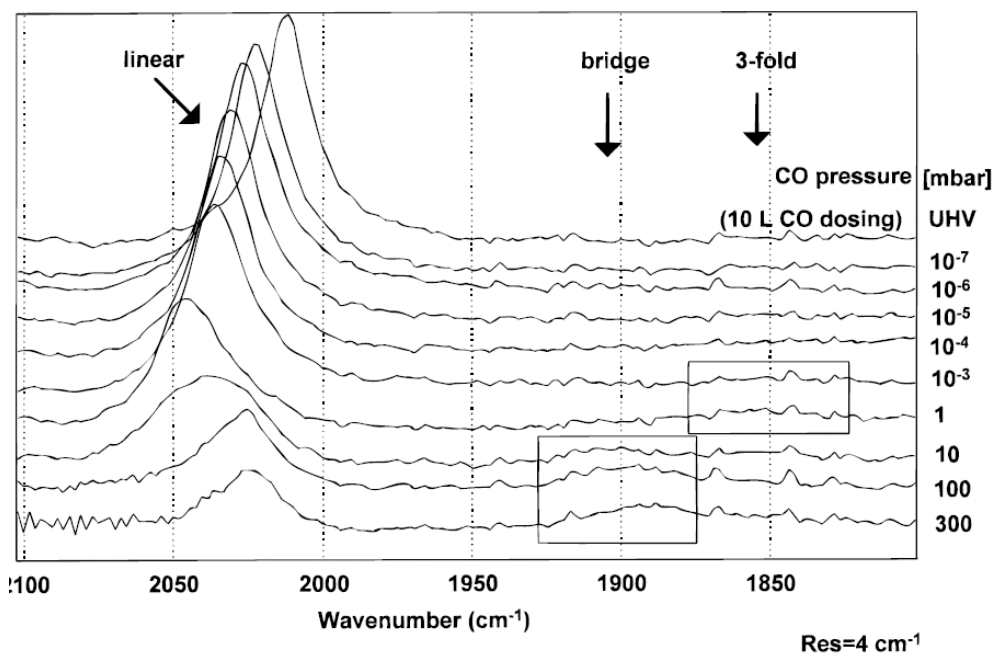


Figure 3.2 Series of PM-RAIR spectra taken on an annealed Co(0001) surface at room temperature at subsequently higher CO pressures from UHV (10 langmuirs of CO dose) to 300 mbar. Intensity and peak position of the signal of linearly bound CO change continuously with pressure. Above 10^{-3} mbar of CO, species attached to bridged sites develop. Adapted from [4].

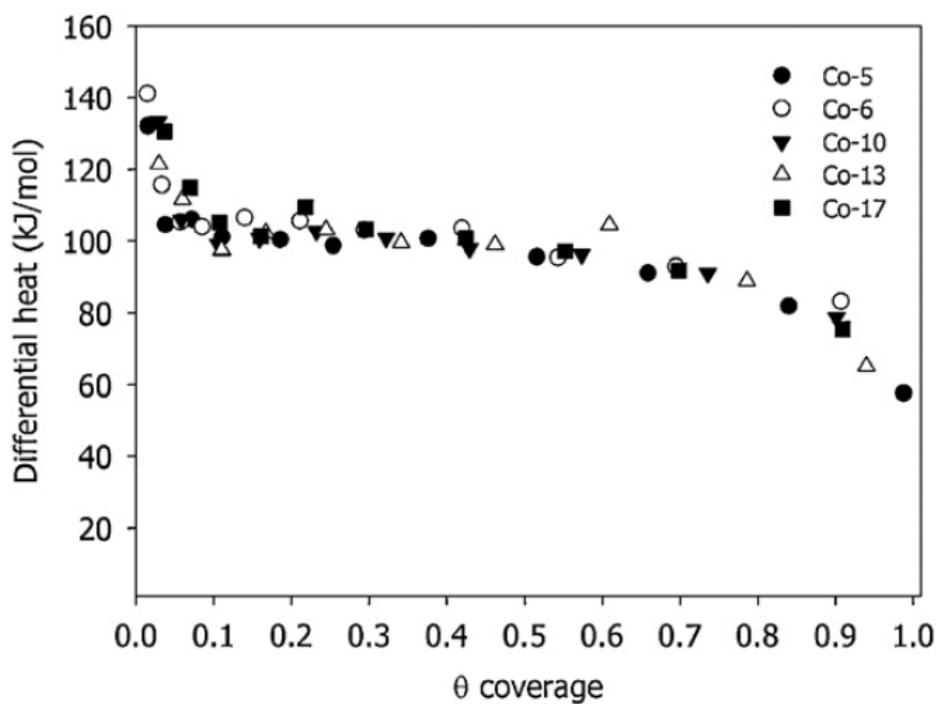


Figure 3.3 Differential heat of CO adsorption at 313 K on 20 wt% Co, with different average cobalt particles sizes. Adapted from [6].

Recent work done by Patanou et al. [8] on supported Co/ γ -Al₂O₃ catalysts and under Fischer-Tropsch conditions, Steady State Isotopic Transient Kinetic Analysis (SSITKA) finds a CO coverage of about 0.5 ML. Patanou et al. [8] further conducted microcalorimetric measurements under Fischer-Tropsch conditions as shown in Figure 3.3.

The present work investigates the adsorption of CO at different coverages on a hcp Co(0001) surface. The possible stable adsorption configurations of CO on Co(0001) terrace surface models are evaluated. Gibbs free energy calculations are then used to determine the equilibrium CO coverage on Co(0001) for various pressures and temperatures. Next, a (p_{CO}, T) phase diagrams on CO on Co(0001) will be established. From the phase diagram, the stable coverage of CO under FT conditions can be determined. Natural Bond Orbitals (NBO) are used to study the bonding of CO on Co(0001) and Bader charges are computed to quantify the effect of charge transfer on bonding.

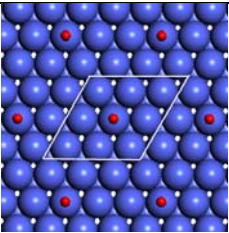
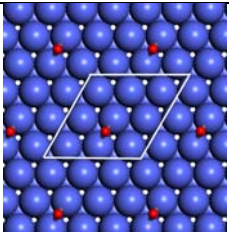
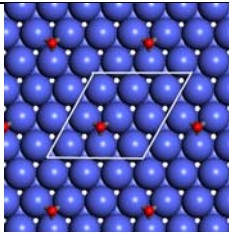
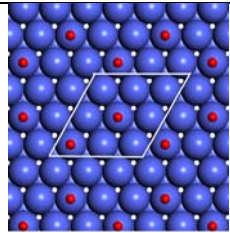
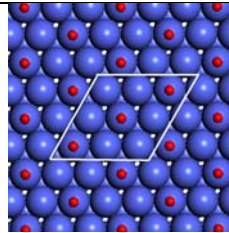
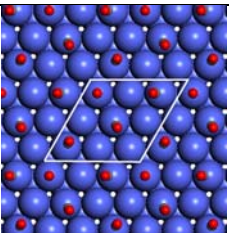
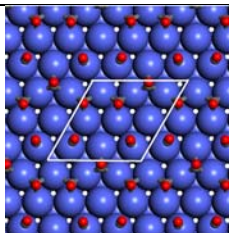
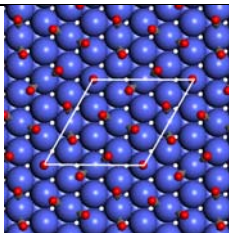
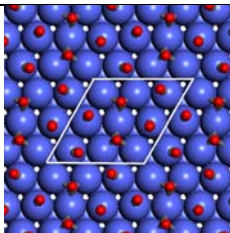
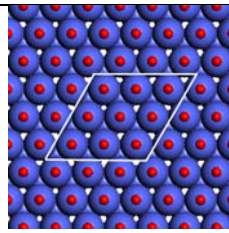
3.2 Results and discussions

3.2.1 Low coverage CO adsorption

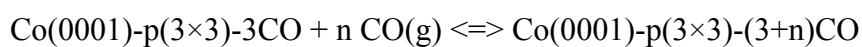
Table 3.1 summarizes the optimized structures and the corresponding adsorption energies. At a low CO coverage of 1/9 ML, an adsorption energy of -130 kJ/mol is calculated for the top sites, in good agreement with the experimental low coverage CO adsorption enthalpy of -128 kJ/mol [2]. CO remains rather mobile and the entropy of adsorbed CO is fairly high at 54 J/mol K. At 300 K and 1 mbar the Gibbs free energy of adsorption is hence very favourable, -82 kJ/mol, and even at 10^{-3} mbar the temperature needs to be increased to 710 K to bring the Gibbs free energy of adsorption to 0 kJ/mol and begin to favour CO desorption.

The top site is found to be the preferred adsorption site, in agreement with experiments [1], and the hollow site is 7 kJ/mol less stable. The difference in adsorption energy between the top and hollow site is somewhat smaller than the difference obtained from empirically corrected DFT-PBE calculations, 14 kJ/mol [9]. Predictions of the correct site preference and of accurate CO adsorption energies are important challenges for DFT [10, 11]. Many studies have shown that conventional DFT functionals overestimate the CO adsorption energy on transition metal surfaces, and favour hollow sites over top sites, in contradiction with experimental data. The overbinding and the incorrect site preference have been attributed to the small CO 5σ - $2\pi^*$ HOMO-LUMO gap in DFT, leading to an overestimation of the backdonation to the $2\pi^*$ LUMO.

Table 3.1 Average and differential^a CO adsorption energies, average Gibbs free adsorption energies (300 K, 1 mbar CO) (kJ/mol) and average entropy (J/mol K) of adsorbed CO for different configurations and coverages on Co(0001).

| | | | | |
|--|--|--|---|--|
|  |  |  |  |  |
| 1/9 - top | 1/9 - bridge | 1/9 - hcp | 2/9 - top | 1/3 - top |
| | | | | ($\sqrt{3} \times \sqrt{3}$)-CO |
| -130/-65/54 | -119/-55/53 | -123/-59/53 | -132/-67/53 | -135/-70/52 |
|  |  |  |  |  |
| 4/9 - top | 5/9 - Optimized | 7/12 | 2/3 - Optimized | 1ML - top |
| | | ($2\sqrt{3} \times 2\sqrt{3}$)-7CO | | |
| -109/ -31 ^a /-42/49 | -104/ -58 ^a /-36/40 | -112/ -75 ^a /-43/39 | -87/-16/36 | +14/+90/25 |

^aDifferential adsorption energy for the adsorption of CO beyond 1/3 ML:



The DFT-revPBE-vdW-DF HOMO-LUMO gap, 7.02 eV, is however slightly larger than the DFT-PBE gap, 6.89 eV, and closer to a DFT+U value, 7.3 eV, [11] where the U parameter was fitted to reproduce the experimental adsorption energy and site preference. The Co cohesive energy in DFT-revPBE-vdW, 483 kJ/mol, falls between the DFT-PBE value, 543 kJ/mol, and the experimental value, 428 kJ/mol [12].

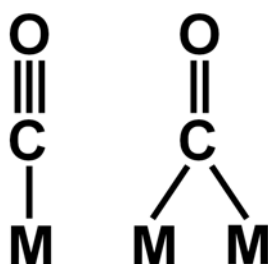


Figure 3.4 Lewis structure resulting from the NBO analysis for CO adsorbed at a top site and CO at a bridge site on Co(0001).

The bonding of CO on Co(0001) was analyzed using the occupancies of the NBOs (Table 3.2). NBO analysis of CO at the top site yields a structure with a single Co-C bond and a triple C-O bond (Figure 3.4), as expected. At the bridge site, NBO finds 2 Co-C and 2 C-O bonds with occupancies above 1.9, again as expected (Figure 3.4). While the bonding Co-C and C-O orbitals are essentially doubly occupied (occupancies >1.9 electrons), the corresponding anti-bonding orbitals also have significant occupancies. At the top site, the anti-bonding Co-C NBO contains 0.36 electrons (Table 3.2). The partially filled anti-bonding Co-C NBO corresponds to Pauli repulsion, and an increase in occupancy weakens the Co-CO bond [13]. Backdonation to the CO $2\pi^*$ orbitals can be quantified from the occupancy of the $2\pi^*$ NBOs (Table 3.2).

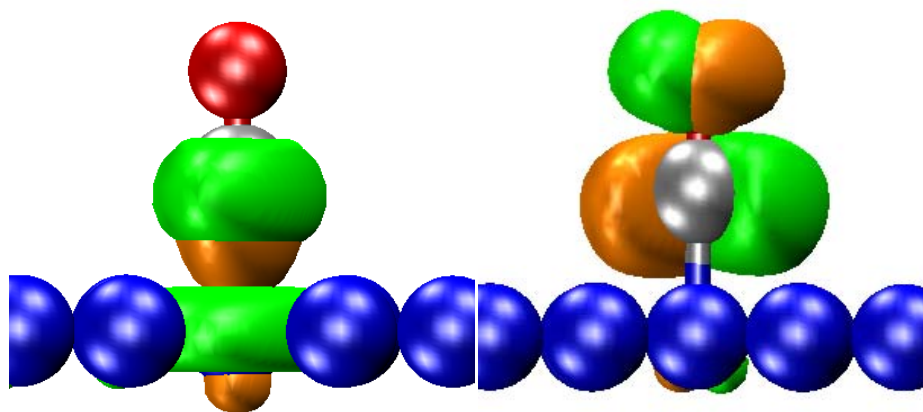


Figure 3.5 Co-C anti-bonding NBO and C-O $2\pi^*$ NBO for CO adsorbed at a top site, 1/3 ML.

An increase in backdonation increases the C-O bond length and strengthens adsorption. The $2\pi^*$ occupancy at the top site in DFT-PBE, 0.290, is higher than in DFT-revPBE-vdW-DF, 0.286, in line with the overestimated backdonation by DFT-PBE. The occupancy of the anti-bonding Co-C NBO in DFT-PBE, 0.329, is much lower than in DFT-revPBE-vdW value, 0.358, again in line with the smaller HOMO-LUMO gap and the stronger adsorption energy, -163 kJ/mol, in DFT-PBE.

Table 3.2 Average CO adsorption energy (kJ/mol), C-O and Co-C distances (Å), CO stretch frequency (cm⁻¹), occupancy of the anti-bonding Co-C NBO and of the C-O 2π* NBO for key CO structures on Co(0001).

| Coverage | 1/9 ML, top | 1/9 ML, bridge | 1/3 ML, top | 7/12 ML |
|---|-------------|-----------------|-----------------|---|
| Adsorption energies (kJ/mol) | -130 | -119 | -135 | -112 |
| d(C-O)/ d(Co-C) (Å) | 1.171/1.765 | 1.189/ 1.927 | 1.169/ 1.763 | Top: 1.161/1.776 Bridge: 1.183/1.879- 1.949 |
| Frequency (cm ⁻¹) | 1936 | 1780 | 1965 | Top: 1985 Bridge: 1790-1860 |
| Antibonding Co-C NBO occupancy ^a (electrons) | 0.358 | 0.440, | 0.342 | Top: 0.453 Bridge: 0.402, 0.363 |
| CO 2π* NBO occupancy ^a (electrons) | 0.286, | 0.393 | 0.277, | Top: 0.285, 0.285 Bridge: 0.376 |
| | 0.286 | | 0.277 | |

^aNBO occupancies are calculated for a monolayer Co(0001) structure, using the geometry optimized on a 5 layer slab.

The effect of the CO coverage on the adsorption energy is evaluated next. Several configurations and adsorption sites were considered for each coverage, and only the most stable structures are included in Table 3.1. For a coverage of 1/3 ML, the $(\sqrt{3}\times\sqrt{3})R30^\circ$ -CO structure is the most stable structure, in agreement with experiments [14]. The adsorption energy of -135 kJ/mol also agrees with experimental values [2]. Interestingly, adsorption becomes *stronger* by 5 kJ/mol when the coverage increases from 1/9 to 1/3 ML (Table 1), and the interactions between neighbouring CO molecules in the $(\sqrt{3}\times\sqrt{3})R30^\circ$ -CO structure are *attractive*. A similar attractive interaction was not found with DFT-revPBE or DFT-PBE calculations [9], or for CO on Pt(111).

The attractive CO-CO interactions suggest that for an overall coverage well below 1/3 ML, isolated $(\sqrt{3}\times\sqrt{3})R30^\circ$ -CO islands are formed. To elucidate the origin of these attractive interactions, we computed NBO occupancies for the 1/9 and 1/3 ML structure (Table 3.2). Note that for the CO-CO distance in the $(\sqrt{3}\times\sqrt{3})R30^\circ$ structure the through-space repulsion is small at only 3 kJ/mol. NBO shows a 0.009 decrease in backdonation to the $2\pi^*$ orbital when the coverage increases from 1/9 to 1/3 ML. The reduced backdonation causes a small decrease in the C-O bond length and a redshift in the CO stretch frequency by 29 cm^{-1} . The dominant factor is however the decrease in the occupancy of the anti-bonding Co-C NBO by 0.016 electrons. The corresponding reduction in the Pauli repulsion explains the stronger Co adsorption at neighbouring Co sites. The reduced occupancy is also reflected

in a slight decrease in the Co-C bond length (Table 3.2). The reduced Pauli repulsion at neighbouring Co sites can be understood from the change in the

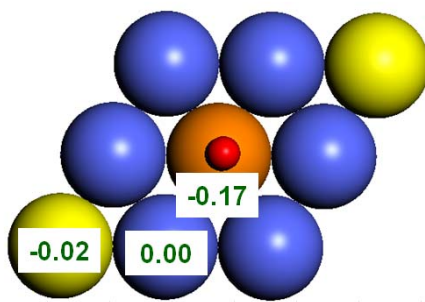


Figure 3.6 Change in the Co(0001) surface Bader charges after CO adsorption at the central Co atom of a $p(3 \times 3)$ unit cell. The central Co atom (orange) loses 0.17 electrons, while the adsorbed CO gains 0.26 electrons. Co atoms along the long diagonal (yellow) lose 0.02 electrons while the Co atoms surrounding the adsorption site remain unchanged. The reduced electron density at the diagonal Co atoms reduces Pauli repulsion with the CO LP NBO and reduces backdonation to the $2\pi^*$ CO orbitals (Table 3.2). The reduced Pauli repulsion in turn strengthens the adsorption at those sites (Table 3.1)

Bader charges of the surface Co atoms after adsorption of a single CO molecule in a $p(3 \times 3)$ unit cell (Figure 3.6). Adsorption increases the charge on CO by 0.26 electrons and reduces the charge on the surface Co atom where CO is adsorbed by 0.17 electrons. The reduced charge on the Co atom causes a redistribution of the charges of surrounding surface Co atoms. Interestingly, the charge on the nearest Co atoms does not change significantly, however, the next-nearest Co atoms lose 0.02 electrons (Figure 3.6). The reduced charge on these Co atoms reduces the Pauli repulsion as well as the backdonation, as found in the NBO analysis.

3.2.2 High coverage CO adsorption

Adsorption of an additional CO in the $(\sqrt{3}\times\sqrt{3})R30^\circ$ structure (3/9 ML) is unfavourable. The differential adsorption energy for 4/9 ML is only -31 kJ/mol (Table 1), too weak to overcome the adsorption entropy penalty of 168 J/mol K. The Gibbs free adsorption energy for an additional CO is hence +24 kJ/mol at 300 K and 1 mbar and the Co(0001) surface seems saturated for a CO coverage of 1/3 ML at these conditions. Also for 5/9 ML, the adsorption energy is too weak to increase the CO coverage beyond 1/3 ML at 300 K and 1 atm. Note that for 5/9 ML, CO occupies both hollow and top sites in the most stable configuration.

In addition to the stable $(\sqrt{3}\times\sqrt{3})R30^\circ$ -CO configuration found in the calculations, surface science experiments have also observed a high coverage $(2\sqrt{3}\times2\sqrt{3})R30^\circ$ -7CO configuration at sufficiently high CO pressure and low temperature. The calculated average adsorption energy for this structure, -112 kJ/mol, is stronger than for a coverage of 4/9 or 5/9 ML. The $(2\sqrt{3}\times2\sqrt{3})R30^\circ$ -7CO configuration is hence a local minimum in the Gibbs free energy as a function of coverage.

3.2.3 CO adsorption Gibbs free energy diagram

A plot of the Gibbs free adsorption energy per surface Co atom for the different coverages as a function of the CO pressure (Figure 3.4), indeed demonstrates that at 300 K, the surface undergoes a phase transition from the $(\sqrt{3}\times\sqrt{3})R30^\circ$ -CO phase to the $(2\sqrt{3}\times 2\sqrt{3})R30^\circ$ -7CO at 0.2 mbar, and that none of the intermediate structures are stable at any pressure. This explains why only two structures have been observed experimentally. The insert furthermore shows that for low coverages only the clean surface and the $(\sqrt{3}\times\sqrt{3})R30^\circ$ -CO structure are the stable phases, and other coverages, i.e., ordered 1/9 ML and 2/9 ML structures, are thermodynamically unstable.

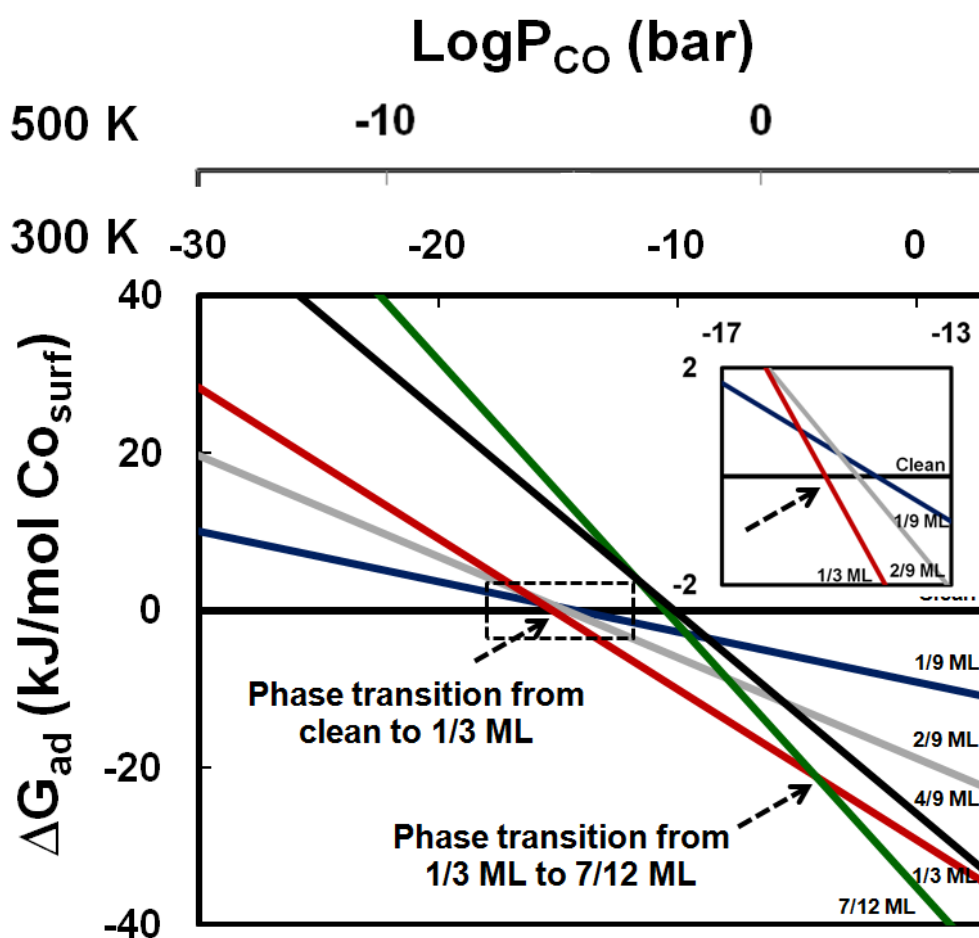
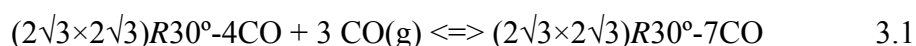


Figure 3.7 Gibbs free energy of CO adsorption per Co(0001) surface area (kJ/mol Co surface atoms) as a function of pressure at 300 K and 500 K for the various structures in Table 3.1. Only two stable phases are found: a low coverage ($\sqrt{3}\times\sqrt{3}$)R30°-CO phase and a high coverage ($2\sqrt{3}\times 2\sqrt{3}$)R30°-7CO phase. All other structures have a significantly higher ΔG_{ad} .

To determine the pressure and temperature for the phase transition from 1/3 ML to 7/12 ML, we computed the Gibbs free energies for reaction (1) as a function of pressure and temperature. The resulting phase diagram is shown in Figure 3.8.



The reaction enthalpy for this reaction, -90 kJ/mol, agrees well with the experimental high coverage adsorption energy, -96 kJ/mol [2]. The entropy of the adsorbed CO, 43 J/mol K at the top sites, is significantly lower than the low coverage value, 54 J/mol K, reflecting the lower mobility. Also for the bridge site the entropy decreases from 53 at 1/9 ML to 40 J/mol K at 7/12 ML.

The phase diagram in Figure 3.8 shows that at low pressures and high temperatures, the $(\sqrt{3}\times\sqrt{3})R30^\circ$ -CO structure is the stable phase, possibly existing as isolated $(\sqrt{3}\times\sqrt{3})R30^\circ$ -CO islands at extremely low pressures (Figure 3.7). When the pressure is increased, a first-order phase transition to the $(2\sqrt{3}\times 2\sqrt{3})R30^\circ$ -7CO configuration is predicted. At 300 K, this transition is occurs at 0.2 mbar. The transition pressure is very sensitive to the calculated reaction enthalpy and entropy for reaction (1). A +10 kJ/mol increase in the reaction enthalpy shifts the transition pressure at 300 K from 0.2 mbar to 12.4 mbar. Similarly, a +10 J/mol K change in the reaction entropy shifts the transition pressure from 0.2 mbar to 0.1 mbar. Our first principle phase diagram can be compared with several experimental data points which are included in Figure 3.8. E.g., using PM-RAIRS Beitel et al. observed the

$(\sqrt{3}\times\sqrt{3})R30^\circ$ structure with CO at the top sites for pressures up to 1 mbar and at room temperature. These conditions indeed fall within the phase domain of the $(\sqrt{3}\times\sqrt{3})R30^\circ$ -CO structure (Figure 3.8). When the CO pressure was increased to 300 mbar, a transition to a $(2\sqrt{3}\times2\sqrt{3})R30^\circ$ structure was observed [29]. These conditions fall within the $(2\sqrt{3}\times2\sqrt{3})R30^\circ$ -7CO region of the stability diagram (\bullet). When the temperature was subsequently increased, the $(2\sqrt{3}\times2\sqrt{3})R30^\circ$ structure transformed back to the $(\sqrt{3}\times\sqrt{3})R30^\circ$ structure above 490 K (\blacktriangle), [30] again consistent with our phase diagram. The stability diagram hence allows to determine the dominant surface structure for different (p_{CO}, T) conditions. For temperatures and CO pressures during FT synthesis, the $(\sqrt{3}\times\sqrt{3})R30^\circ$ -CO structure is found to be the most stable structure (\blacksquare , Figure 3.8). The stability of a saturated phase under reaction conditions is furthermore consistent with an observed CO reaction order close to zero in Fischer-Tropsch synthesis under these conditions, even though the measured CO coverage is significantly less than 1 ML [13,23]. As discussed above, once the $(\sqrt{3}\times\sqrt{3})R30^\circ$ -CO structure has formed, adsorption of additional CO molecules is unfavourable, and the surface is saturated with CO. Also for the 7/12 ML phase, adsorption of additional CO is unfavourable, except at very high pressures (Figure 3.7).

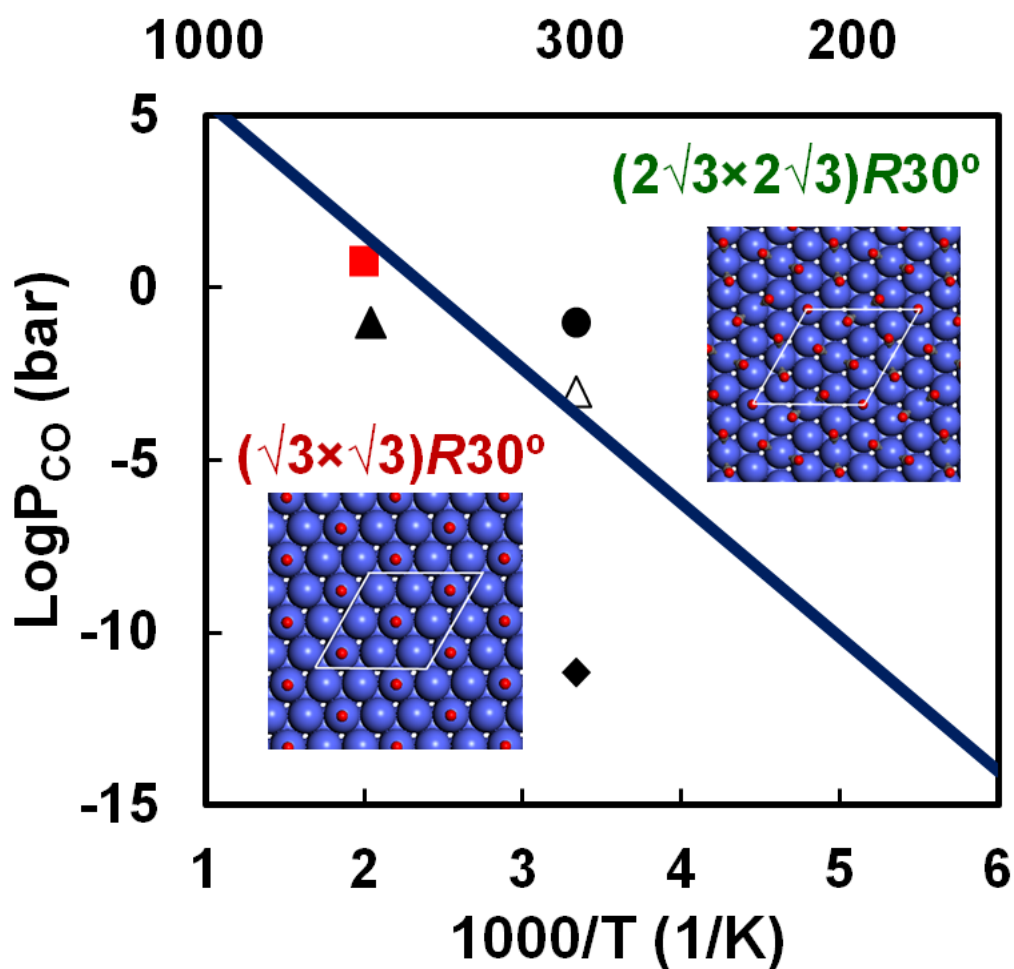


Figure 3.8 First principle phase diagram for CO adsorption on Co(0001). The two stable phases (Figure 3.1) are separated by a first-order phase transition (line). Both structures are shown and the CO adsorption enthalpies and Gibbs free energies are summarized in Table 3.1. Both structures have been observed experimentally and the conditions where each structure was observed are indicated. (♦) $(\sqrt{3}\times\sqrt{3})R30^\circ$ -CO structure at 7×10^{-9} mbar and 300 K (Bridge et al. [1]). (Δ) $(\sqrt{3}\times\sqrt{3})R30^\circ$ -CO structure below 1 mbar and at 300 K (Beitel et al. [4]). (▲) $(\sqrt{3}\times\sqrt{3})R30^\circ$ -CO structure at 100 mbar and 490 K (Beitel et al. [5]). (●) $(2\sqrt{3}\times 2\sqrt{3})R30^\circ$ -7CO structure at 100 mbar and 300 K (Beitel et al. [5]). (■) Typical FT synthesis conditions: 6 bar and 500 K[15].

4.3 Conclusions

In conclusion, CO adsorption on Co(0001) was studied with DFT-revPBE-vdW-DF. With this approach, the correct top site preference and accurate adsorption energies are predicted. Two stable phases were found: a low coverage $(\sqrt{3}\times\sqrt{3})R30^\circ$ -CO phase and a high coverage $(2\sqrt{3}\times2\sqrt{3})R30^\circ$ -7CO phase, separated by a first order phase transition. The temperature and pressure of the first-order phase transition agree well with available experimental data. Experimentally, phase transitions are characterized by a discontinuity in the physical properties and modern micro-calorimetric methods [16] might be able to directly observe the predicted phase transition. At coverages below 1/3 ML, the calculations suggest the formation of isolated $(\sqrt{3}\times\sqrt{3})R30^\circ$ -CO islands due to the attractive interactions between neighbouring CO molecules. The stability of the various surface structures was analyzed using the changes in the occupancies of the anti-bonding NBOs, providing a quantitative analysis of the variation in the CO adsorption energy.

4.4 References

- [1] M.E. Bridge, C.M. Comrie, R.M. Lambert, *Surf. Sci.*, 67 (1977) 393.
- [2] H. Papp, *Surf. Sci.*, 129 (1983) 205.
- [3] J.J.C. Geerlings, M.C. Zonneville, C.P.M. de Groot, *Surf. Sci.*, 241 (1991) 302.
- [4] G.A. Beitel, A. Laskov, H. Oosterbeek, E.W. Kuipers, *J Phys Chem-US*, 100 (1996) 12494.
- [5] G.A. Beitel, C.P.M. de Groot, H. Oosterbeek, J.H. Wilson, *The Journal of Physical Chemistry B*, 101 (1997) 4035.
- [6] E. Patanou, E.Z. Tveten, D. Chen, A. Holmen, E.A. Blekkan, *Catal. Today*, 214 (2013) 19.
- [7] J. Lahtinen, J. Vaari, K. Kauraala, E.A. Soares, M.A. Van Hove, *Surf. Sci.*, 448 (2000) 269.
- [8] J.P. den Breejen, P.B. Radstake, G.L. Bezemer, J.H. Bitter, V. Frøseth, A. Holmen, K.P.d. Jong, *J. Am. Chem. Soc.*, 131 (2009) 7197.
- [9] M. Zhuo, A. Borgna, M. Saeys, *J. Catal.*, 297 (2013) 217.
- [10] P.J. Feibelman, B. Hammer, J.K. Nørskov, F. Wagner, M. Scheffler, R. Stumpf, R. Watwe, J. Dumesic, *The Journal of Physical Chemistry B*, 105 (2001) 4018.
- [11] G. Kresse, A. Gil, P. Sautet, *Physical Review B*, 68 (2003) 073401.
- [12] W.M. Haynes, *CRC Handbook of Chemistry and Physics*, 95th Edition ed., CRC Press, Boca Raton, 2014-2015.
- [13] Y.P.G. Chua, G.T.K.K. Gunasooriya, M. Saeys, E.G. Seebauer, *J. Catal.*, 311 (2014) 306.
- [14] G. Ertl, M. Neumann, K.M. Streit, *Surf. Sci.*, 64 (1977) 393.

[15] B.H. Davis, M.L. Occelli, Fischer–Tropsch Synthesis, Catalysts and Catalysis, Elsevier B.V., 2007.

[16] J.-H. Fischer-Wolfarth, J. Hartmann, J.A. Farmer, J.M. Flores-Camacho, C.T. Campbell, S. Schauermaun, H.-J. Freund, Rev. Sci. Instrum., 82 (2011).

Chapter 4

CO adsorption on platinum: accurate prediction of site preference and analysis of the change in site preference at high coverage

4.1 Introduction

The adsorption of CO on platinum surfaces has received continued interest ever since Langmuir studied this system [1] and has been studied extensively in the past century due to its importance in understanding CO oxidation in automotive exhausts and use as anode catalysts for direct methanol fuel cells. In general, CO on Pt is considered as a model system in the field of surface science [2]. Wide ranges of experimental techniques and theoretical studies have been employed to understand the CO adsorption on platinum surfaces.

Low energy electron diffraction (LEED) [3, 4], thermal desorption spectroscopy (TDS) [3, 4], work function measurements [3], electron energy loss spectroscopy (EELS) [4, 5], molecular beam scattering [6], reflection-absorption infrared spectroscopy (RAIRS) [7-9] are some of the experimental techniques that have been used.

For low coverage, calorimetric studies on single crystals lead to measured heats of adsorption of 138 kJ/mol [10] as does isosteric heat measurement [3]. TPD studies have provided slightly lower values of 122 kJ/mol [11] and 130 kJ/mol [12]. On the other hand, calorimetric studies on thin films by King et al. [13, 14] reported a rather high value of 183 kJ/mol.

At low coverages, CO adsorbs at the top sites [15-20] and diffusion to the less stable bridge sites faces an energy barrier, as illustrated in Figure 4.1. Different models have been used to extract the potential energy surface for CO on Pt(111) from experimental data.

Steinrück et al. [21] showed that the ratio of the on-top and bridge population for a certain total coverage during CO uptake should depend on the incoming particle flux. In the limit of very low pressures, the site exchange fluxes in Figure 4.1 are much higher than the adsorption flux, which means that the site occupations are very close to thermal equilibrium.

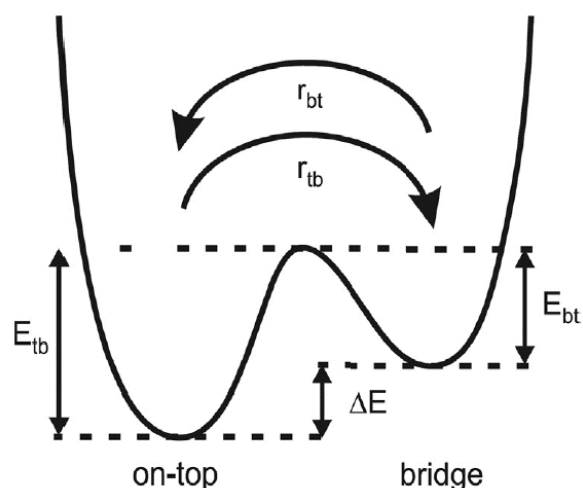


Figure 4.1 Potential energy surface for diffusion from the top to the bridge site. ΔE is the energy difference between the two sites, E_{tb} and E_{bt} are activation energies for site exchange and r_{bt} , r_{tb} the site exchange rates. Adapted from [22].

Figure 4.2 shows the on-top and bridge coverages and the total coverage (sum of on-top and bridge) as a function of exposure, measured at 200 K with different sample pressures [22]. The data show that first on-top and later also bridge sites are populated. Around ~ 1.6 L, the coverage of 0.50 ML of the $c(4 \times 2)$ structure is reached. This indicates that the structure builds up gradually to 0.5 ML without forming any intermediate phases under these conditions. At higher exposures, the increase in coverage significantly slows down. As can be seen from Figure 4.2, at least up to a total coverage of 0.35 ML (about 0.9 L) the data obtained at different pressures are in perfect agreement, indicating that the site occupation is independent of pressure.

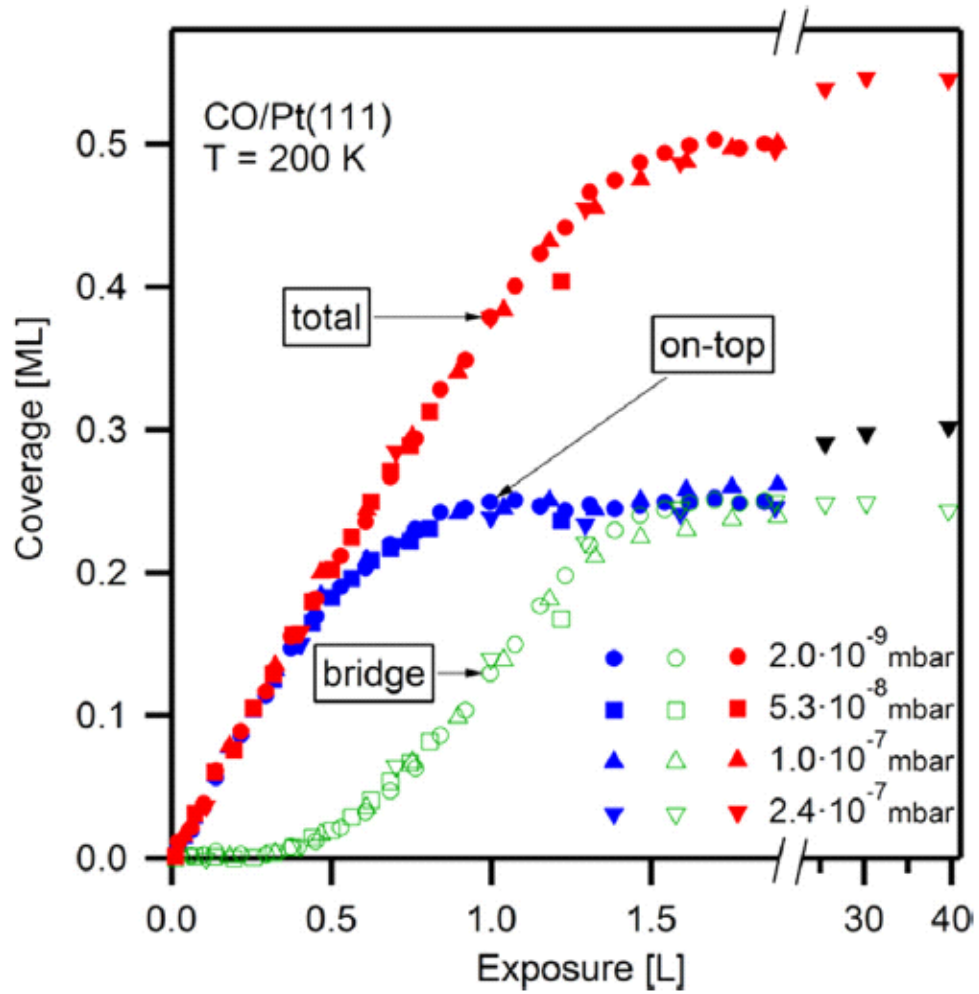


Figure 4.2 CO coverage on Pt(111) vs. exposure at T=200 K for different pressures 2.0×10^{-9} , 5.3×10^{-8} , 1.0×10^{-7} , 2.4×10^{-7} mbar. Blue symbols: top, open green symbols: bridge, red symbols: total coverage. Adapted from [22].

As the two adsorption sites (top and bridge) are in thermal equilibrium with each other, Kinne et al. [22] used temperature-dependent adsorption experiments to derive the binding energy difference, ΔE , between CO adsorbed at on-top and bridge sites. Their model yields a $\Delta E=41$ meV, but ignored the lateral interactions within the CO layer. A much more advanced approach was put forward by McEwen et al. [23], who developed a comprehensive theory of the adsorption of CO on Pt(111) to describe equilibrium properties as well as the adsorption and desorption kinetics known from literature. It is based on a multi-site lattice gas model, which allows for adsorption at on-top and bridge sites, and includes site exclusion and lateral interactions out to second neighbour unit cells as well as a mean field to account for long ranged dipole interactions between CO molecules. From this thermodynamic model including several parameters, a ΔE of 95 meV was estimated.

For low coverages, LEED studies show rather diffuse $(\sqrt{3}\times\sqrt{3})R30^\circ$ diffraction structure with CO at top sites (Figure 4.3) at 300 K and for an exposure of 1 L. Once the temperature is lowered to 170 K the diffraction patterns became more intense and sharper.

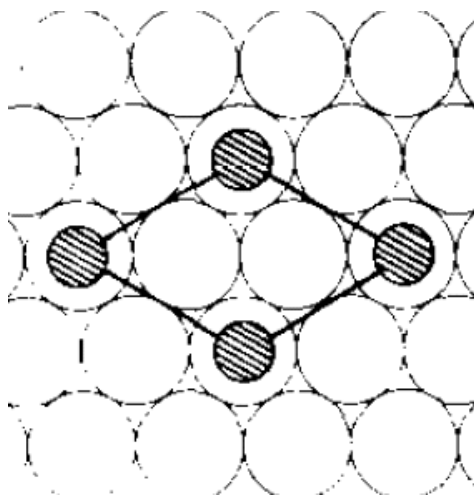


Figure 4.3 Schematic representation of the $(\sqrt{3} \times \sqrt{3})R30^\circ$ structure with CO adsorption at top sites on Pt(111). Adapted from [5].

At 0.5 ML coverage, LEED studies show a well ordered $c(4 \times 2)$ pattern (Figure 4.4) at temperatures lower than 300 K [4]. Electron energy loss spectroscopy [4, 5], infrared reflection adsorption spectroscopy [24, 25], He scattering [26] and X-ray photoemission spectroscopy (XPS) [27] indicate the coexistence at of two inequivalent CO molecules on the surface, with a C 1s binding energy difference of 0.7 eV, identified as atop and bridge adsorption sites.

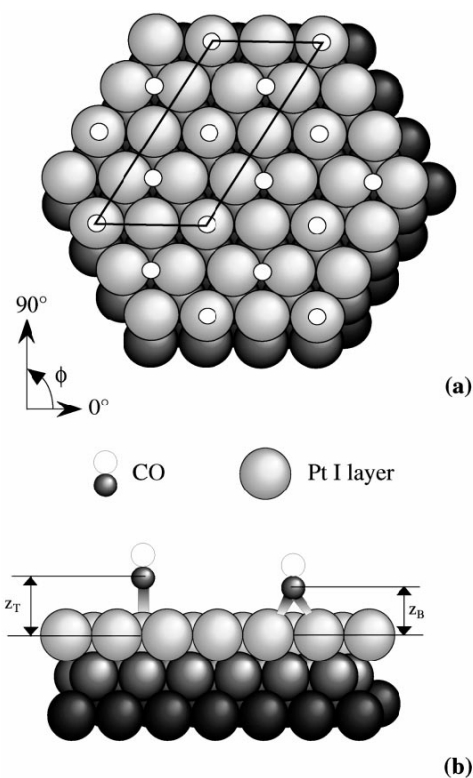


Figure 4.4 Schematic representation of the $c(4 \times 2)$ -2CO structural model: 1) top view b) side view. Adapted from [28].

Above 0.5 ML, surface crowding and CO-CO repulsion has been suggested to lead to tilted CO molecules on Pt(111). Kiskinova et al. [29] measured electron stimulated desorption ion angular distributions (ESDIAD) to study high CO coverages on Pt(111). Three species were detected desorbing from the surface. The triplet CO^* and positive ion CO^+ trajectories reflect the Pt-C bond angle while CO^+ trajectories give information about the C-O bonds. The authors demonstrated that high coverage CO/Pt(111) phases are associated with tilted atop CO species with a tilting angle of up to $6 \pm 1^\circ$ from the normal, as indicated by the CO^* species or up to $14 \pm 1^\circ$ as indicated by the CO^+ species. The CO^+ species is strongly influenced by image charge and neutralization effects at large angles and therefore the polar angle of the atop

bonded CO species was concluded to be $\sim 6^\circ$, as indicated by the CO* species [29].

Three different models (Figure 4.5) have been proposed for the $c(\sqrt{3}\times 5)\text{rect-}6\text{CO}$ structure which corresponds to 0.6 ML coverage. Model (a) is proposed by Persson et al. [30], while model (b) is suggested by Avery based on an early EELS study [31]. Avery's model shows denser atop chains and wider-spaced CO molecules in bridging sites. Model (c) proposed by Petrova and Yakovkin [32] is rather different. This model is developed on the basis of a reassessment of the published LEED patterns and kinematical theory (single scattering) modelling of these patterns. The basis of their analysis has been questioned; for example this paper introduces 'missing' diffracted beams for the accepted structure of the Ni(111) $c(4\times 2)\text{-CO}$ phase, an artefact of the kinematic simplification. However, a key feature of this model is that it contains twice as many bridge CO as atop CO molecules, clearly different from the models (a) and (b). As has been mentioned in the introduction, the XPS data of Bjorneholm et al. [27] show that this third model cannot be correct; quantitative XPS shows an atop:bridge occupation ratio of 2:1.

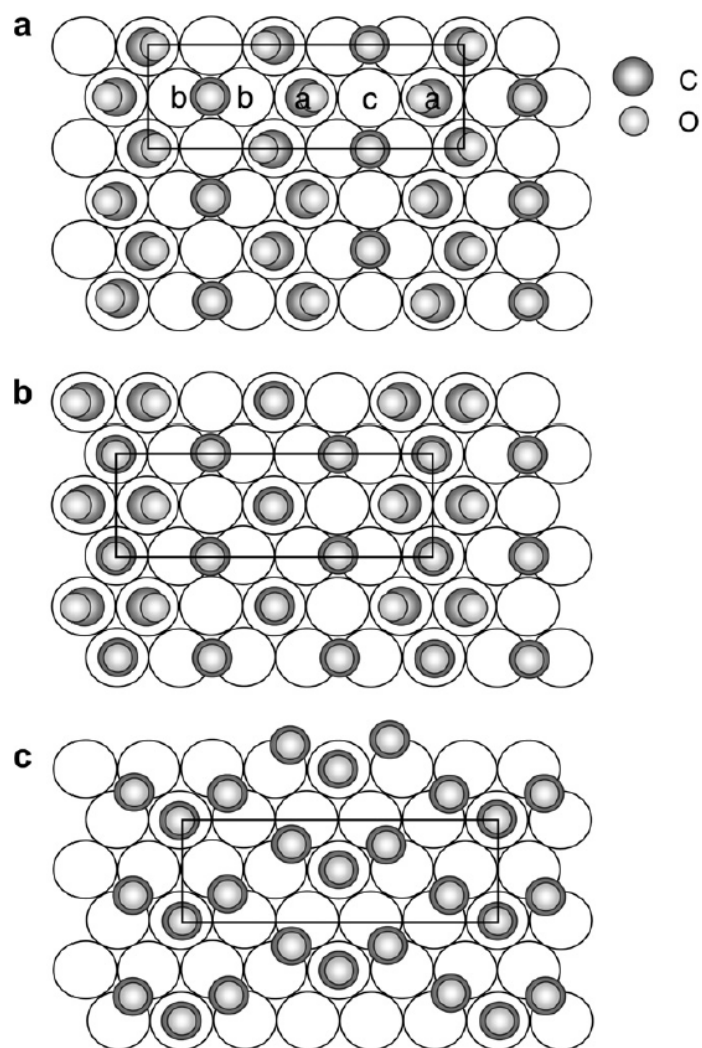


Figure 4.5 Models proposed for the $c(\sqrt{3}\times 5)\text{rect-6CO}$ structure which corresponds to 0.6 ML. (a) Persson et al. (b) Avery et al. (c) Petrova and Yakovkin et al. Adapted from [33].

The present work investigates the adsorption of CO for different coverages on a fcc Pt(111) surface. The possible stable adsorption configurations of CO on Pt(111) terrace surface models are evaluated. Gibbs free energy calculations are then used to determine the equilibrium CO coverage on Pt(111) for a range of pressures and temperatures. In addition, changes in relative stability between bridge and top CO with coverage are explored. Natural Bond Orbitals (NBO) are used to study the bonding of CO on Pt(111) and Bader charges are computed to quantify the effect of charge transfer on bonding.

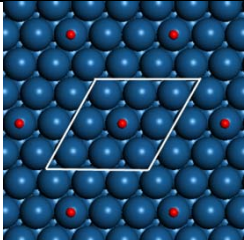
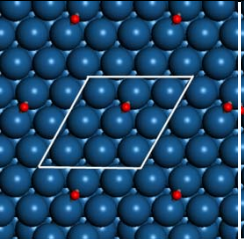
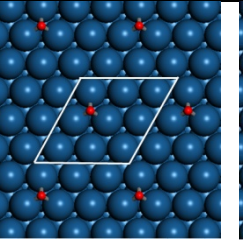
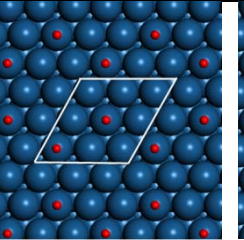
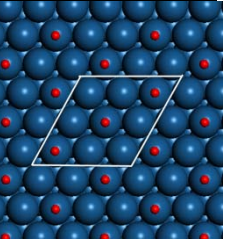
4.2 Results and discussions

4.2.1 Low coverage CO adsorption

Table 4.1 summarizes the optimized structures and the corresponding adsorption energies for low coverage CO adsorption on a 5-layer Pt(111) slab with a $p(3\times 3)$ unit cell. The low coverage DFT-revPBE+vdW adsorption energy of -143 kJ/mol agrees well with the generally accepted experimental value of -138 kJ/mol [3, 10], and the site preference is correctly predicted. At 300 K and 1 mbar, the Gibbs free energy of adsorption (stability) is very favourable. The stability difference between the top and the bridge site for 1/9 ML coverage is 9 kJ/mol. This value agrees well with the energy difference estimated by McEwen et al. [23] based on detailed experimental data using a detailed thermodynamic model. For Co(0001), the 1/9 ML coverage bridge site stability (-55 kJ/mol) is lower than hollow site (-59 kJ/mol). Unlike Co(0001), for Pt(111) the 1/9 ML coverage bridge site stability (-57 kJ/mol) is higher than hollow site (-53 kJ/mol). This indeed indicates why hollow sites are not observed experimentally on Pt(111). The entropy for adsorbed CO on the top site is higher by 10 and 14 J/mol K compared to bridge and hollow site respectively. This higher entropy of CO at the top site is attributed to a higher frustrated translational entropy.

CO adsorption energies for 2/9 ML and 1/3 ML are -142 and -139 kJ/mol respectively. The CO adsorption energy decreases by 4 kJ/mol when the coverage increases from 1/9 to 1/3 ML, and, contrary to Co(0001), on Pt(111) the interactions between adsorbed CO molecules are repulsive. As expected, the entropy for an adsorbed CO decreases with increasing coverage due to reduced mobility.

Table 4.1 Average CO adsorption energies (kJ/mol), average Gibbs free adsorption energies (300 K, 1 mbar CO) (kJ/mol) and average entropy (J/mol K) for different low coverage configurations on a 5-layer Pt(111) slab with a $p(3 \times 3)$ unit cell.

| | | | | |
|--|--|--|---|--|
|  |  |  |  |  |
| 1/9 - top | 1/9 - bridge | 1/9 - hcp | 2/9 - top | 1/3 - top |
| -143/-66/55 | -136/-57/45 | -132/-53/40 | -142/-64/53 | -139/-62/51 |

A Bader charge analysis was performed to analyze the origin of the repulsive interactions (Figure 4.6) similar to the analysis for Co(0001) in Section 3.3.1. Bond lengths, CO stretch frequency and NBO occupancies for 1/9 ML and 1/3 ML coverages are summarized in Table 4.2.

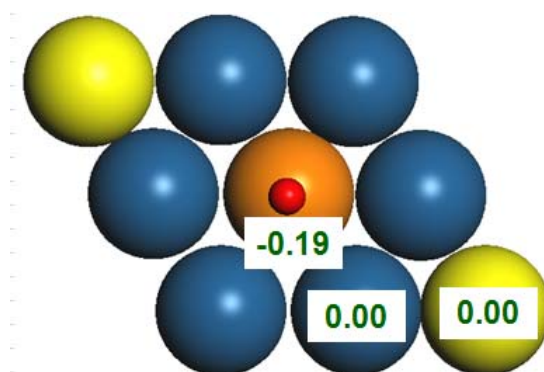


Figure 4.6 Change in the Pt(111)- $p(3\times 3)$ surface Bader charges after CO adsorption at the central Pt atom of a $p(3\times 3)$ unit cell. The central Pt atom (orange) loses 0.19 electrons, while the adsorbed CO gains 0.20 electrons. Charge on the Pt atoms surrounding the adsorption site (blue) and along the diagonal (yellow) remain unchanged, hence adsorption of the next CO on the yellow Pt atom is slightly weaker due to through space repulsion (Tables 4.1 and 4.2).

Addition of a CO molecule to a $p(3\times 3)$ unit cell changes the electron density of the surface Pt atoms as shown in Figure 4.5. The central Pt atom loses 0.19 electrons after CO adsorption, which is more than Co. However, this larger change in the Pt charge does not lead to a larger change in the charge on the surrounding surface Pt atoms as compared to Co. Indeed, their charge remains nearly unchanged. As a result, the occupancy of the $2\pi^*$ NBO of CO adsorbed at the neighbouring Pt atom (yellow in Figure 4.6) remains unchanged and the CO bond length also does not change. Only a small 10 cm^{-1} red-shift in the CO

stretch frequency is calculated. The anti-bonding Pt-C NBO occupancy (corresponding to Pauli repulsion) of the neighbouring CO increases slightly, reducing the adsorption energy. The increased Pauli repulsion also increases the Pt-C bond length from 1.850 Å to 1.860 Å, as shown in Table 4.2. Again this trend is opposite to situation for CO on Co(0001), as discussed in the previous chapter.

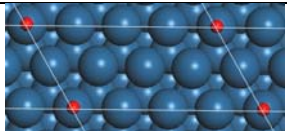
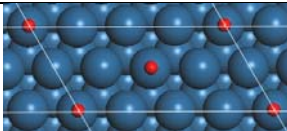
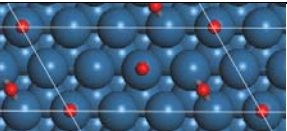
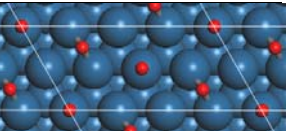
Table 4.2 C-O and Pt-C bond lengths (Å), CO stretch frequency (cm⁻¹), occupancy of the anti-bonding Pt-C NBO and of the C-O 2π* NBO for key CO structures on Pt(111)-p(3x3) unit cell.

| Coverage | 1/9 ML - top | 1/9 ML - bridge | 1/3 ML - top |
|--|--------------|-----------------|--------------|
| d(C-O), d(Pt-C) (Å) | 1.160, 1.850 | 1.184, 2.040 | 1.160, 1.860 |
| Frequency (cm ⁻¹) | 2024 | 1820 | 2033 |
| Anti-bonding Pt-C NBO occupancy (electrons) | 0.51 | 0.47,0.47 | 0.53 |
| CO 2π* NBO occupancy (electrons) | 0.20, 0.20 | 0.22 | 0.20, 0.20 |

4.2.2 High coverage CO adsorption

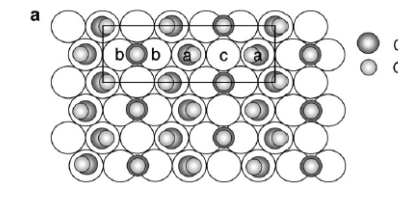
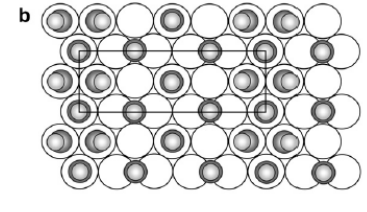
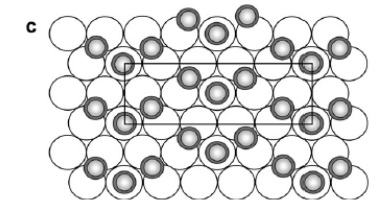
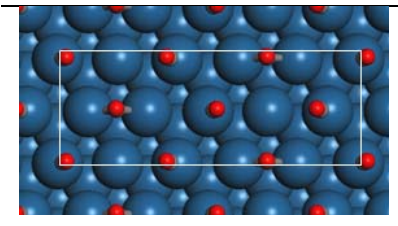
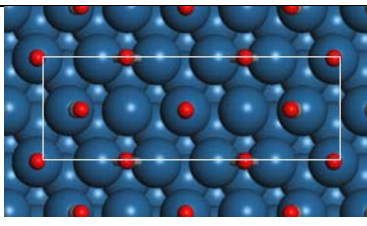
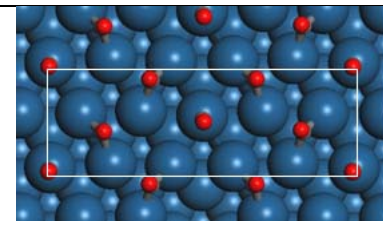
Next, the CO coverage was increased to 0.5 ML (Table 4.3). Low coverage CO adsorption energies and stabilities in a $c(4 \times 2)$ unit cell (1/8 ML) agree well with the low coverage calculations in a $p(3 \times 3)$ unit cell (Table 4.1). With an increase in the CO coverage, adsorption becomes weaker. The most stable configuration, 2T+2B, again agrees with experiments.

Table 4.3 Average CO adsorption energies (kJ/mol), average Gibbs free adsorption energies (300 K, 1 mbar) (kJ/mol), and average entropy of adsorbed CO (J/mol K) for different configurations in a $c(4 \times 2)$ unit cell.

| | | | |
|--|--|---|--|
|  |  |  |  |
| 1/8 - top | 1/4 - top | 3/8 - 2T+1B | 1/2 - 2T+2B |
| -141 / -65/56 | -138 / -61/55 | -137 / -59/49 | -136 / -57/46 |

Increasing the coverage further, we studied CO adsorption in a $(\sqrt{3} \times 5)$ rect unit cell. Avery [31] proposed a $(\sqrt{3} \times 5)$ -6CO and a $(\sqrt{3} \times 3)$ -4CO structure for CO coverages of 0.6 and 0.667 ML, respectively. Evidence for a dense CO overlayer on Pt(111) and for the $(\sqrt{3} \times 5)$ rect and the $(\sqrt{3} \times 3)$ rect structures is provided by high resolution EELS, by temperature programmed desorption and by LEED (Kostov et al. [34] and Biberian et al. [35]).

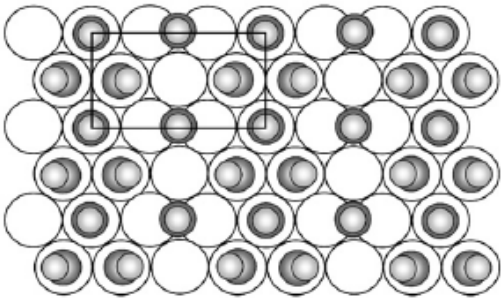
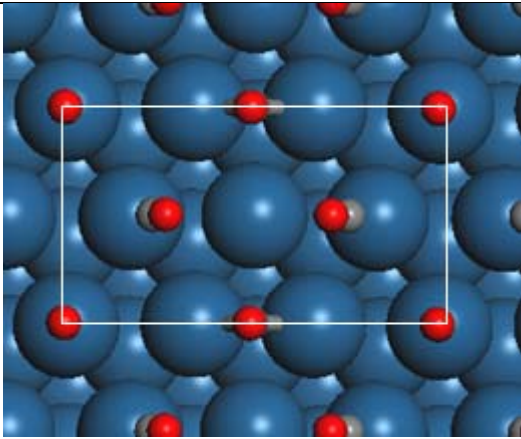
Table 4.4 Average CO adsorption energies (kJ/mol), average Gibbs free adsorption energies (300 K, 1 mbar) (kJ/mol), and entropy of adsorbed CO (J/mol K) for different combinations of bridge and top sites in a ($\sqrt{3}\times 5$)rect unit cell, 0.6 ML.

| | | |
|---|---|--|
|  |  |  |
|  |  |  |
| Persson et al. [30] | Avery et al. [31] | Petrova and Yakovkin et al. |
| 4T+2B | 4T+2B | [32] |
| 2T+4B | | |
| -131/-51/43 | -129/-49/44 | -120/ -40/43 |

Three different configurations have been proposed for the ($\sqrt{3}\times 5$)rect-6CO structure with a coverage of 0.6 ML, with different bridge:top ratios, as explained in section 4.1. A key feature for the structure proposed by Petrova and Yakovkin [32] is that it has 4 bridge CO and 2 top CO per unit cell, while the structures proposed by Persson et al. [30] and by Avery et al. [31] have more top CO than bridge CO. Calculations using the PBE functional (which overestimate the stability of CO at higher coordination sites) therefore support the model proposed by Petrova and Yakovkin (-158 kJ/mol). DFT-revPBE+vdW however favour the structure proposed by Persson et al., in agreement with quantitative XPS data by Bjorneholm et al. [27].

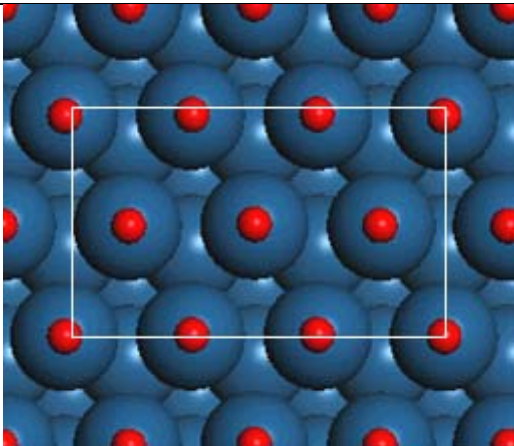
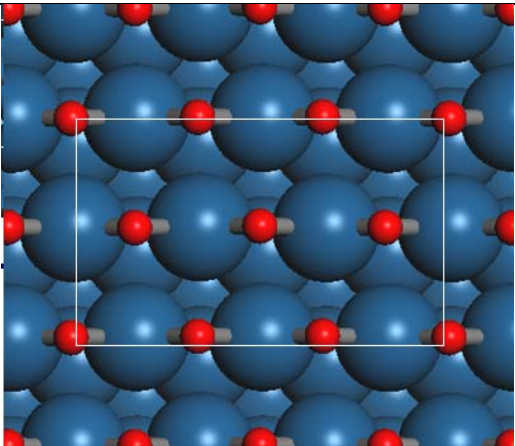
Next, the coverage was increased to 0.67 ML using a ($\sqrt{3}\times 3$)rect unit cell (Table 4.5). Various CO configurations were studied. The most stable configuration has 3 CO at top sites and 1 at the bridge site. Other configurations are shown in Table 4.5 as well. Interestingly, two of the CO molecules are tilted. The calculated adsorption energy of -126 kJ/mol is close to the value reported by calorimetric measurements for a saturated surface, -118 kJ/mol [36], and lower than the value for the 0.6 ML coverage.

Table 4.5 Average CO adsorption energy (kJ/mol), average Gibbs free adsorption energy (300 K, 1 mbar) (kJ/mol) and entropy of adsorbed CO (J/mol K) for a 0.66 ML coverage in a ($\sqrt{3}\times 3$)rect unit cell.

| |
|--|
|  |
|  |
| <hr/> Avery et al. 0.67 ML - 3T+1B -126/-45/42 <hr/> |

Finally, the CO coverage was increased to 1 ML. At this coverage, CO adsorbs on top site of each surface Pt atom as shown in Table 4.6. The structure with CO at the bridge and at the hollow sites is 20 kJ/mol less stable. Unlike Co(0001) where CO adsorption at 1 ML coverage is endothermic, the CO adsorption energy for Pt(111) is still quite favourable at -74 kJ/mol. Still, the CO adsorption energy is insufficient to overcome the adsorption entropy penalty at 300K and 1 mbar (+9 kJ/mol), but adsorption becomes favourable at 1 bar (-19 kJ/mol).

Table 4.6 Average CO adsorption energy (kJ/mol), average Gibbs free adsorption energy (300 K, 1 mbar) (kJ/mol) and entropy of adsorbed CO (J/mol K) for a 1 ML coverage in a ($\sqrt{3}\times 3$)rect unit cell.

| | |
|---|--|
|  |  |
| 1 ML 6T | 1 ML 6B |
| -74/+9/32 | -55/+29/30 |

4.2.3 Stability diagram for CO adsorption Pt(111)

The stability diagram for CO on Pt(111) is constructed in a similar manner to Co(0001). Unlike CO on Co(0001), the CO coverage on Pt(111) increase gradually with pressure up to 1/3 ML. With further increase in coverage, several stable phases are found, (4×2) -4CO [also known as $(\sqrt{3} \times 2)$ rect-2CO], $(\sqrt{3} \times 5)$ rect-6CO, $(\sqrt{3} \times 3)$ rect-4CO, $(\sqrt{3} \times 3)$ rect-6CO.

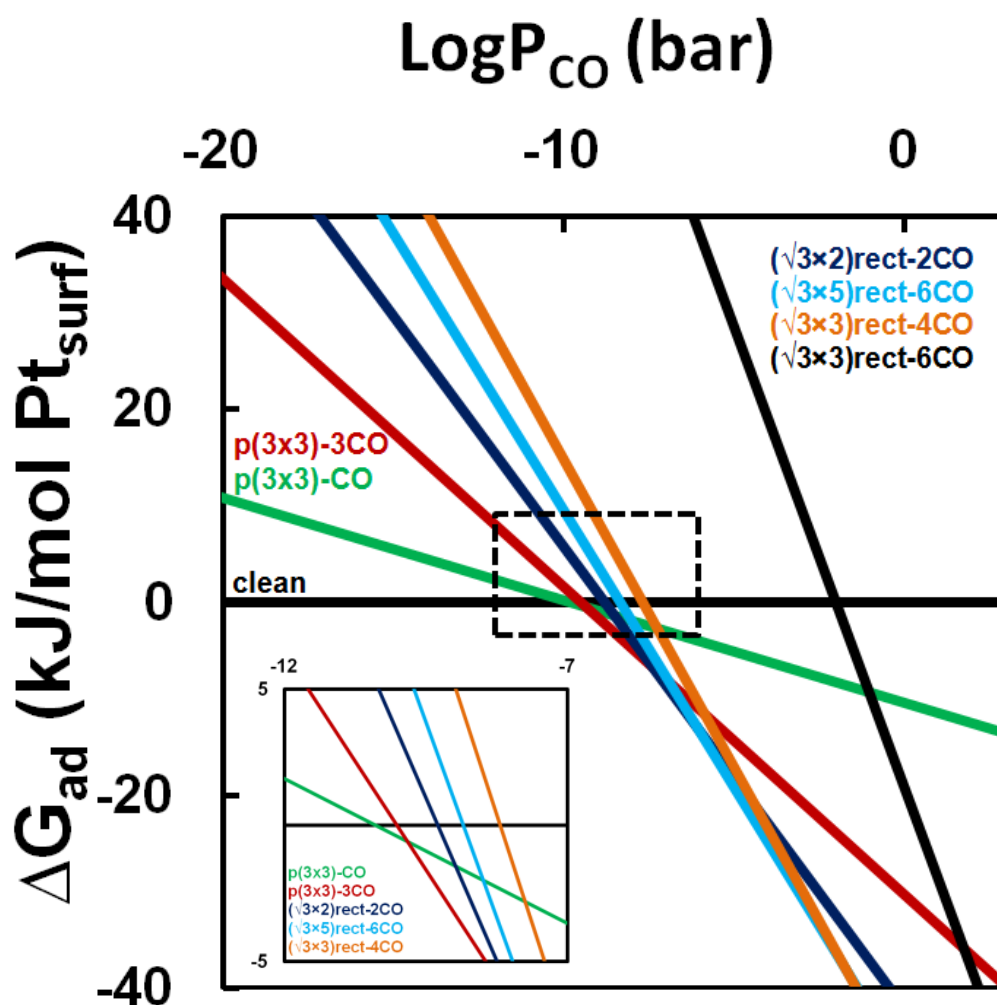


Figure 4.7 Gibbs free energy of CO adsorption per Pt(111) surface area (kJ/mol Pt surface atoms) as a function of pressure at 300 K for the various structures discussed on section 4.2.1 and 4.2.2.

4.2.4 Change in relative stability of on-top CO vs bridge CO with coverage

At low coverages CO adsorption at the top is preferred over the bridge site. Figure 4.2 shows on-top and bridge coverages as a function of exposure, measured at 200 K for different CO pressures. This data show that CO first adsorbs at the on-top sites before adsorption at the bridge sites starts for an exposure of 0.4 L (or a coverage of 0.125 ML).

Around ~ 0.9 L, the top site coverage saturates at 0.25 ML. When the exposure is increased to around ~ 1.6 L, the $c(4 \times 2)$ structure is formed for a coverage of 0.5 ML. The surface is saturated for this coverage at those conditions. DFT calculations show that the stability difference between the top and the bridge site for $1/9$ ML coverage is 9 kJ/mol. In this section, the change in the relative stability of on-top and bridge CO at low coverages (< 0.3 ML) and at high coverages (> 0.5 ML) is discussed. To analyze the low coverage case, the $(\sqrt{3} \times 5)_{\text{rect}}\text{-2CO}$ was studied while the $(\sqrt{3} \times 5)_{\text{rect}}\text{-6CO}$ structure was used for the high coverage case. As shown in Figure 4.8, on a clean surface CO preferably adsorbs at the top site. The adsorption energy difference between top and bridge site is 8 kJ/mol for $1/10$ ML coverage similar to the value at $1/9$ ML coverage (Table 4.1). For the $(\sqrt{3} \times 5)_{\text{rect}}\text{-2CO}$ structure, the differential adsorption energy for the top site decreases from -142 kJ/mol at low coverage to -137 kJ/mol at 0.2 ML while for the bridge site the adsorption energy slightly increases from -134 kJ/mol at low coverage to -135 kJ/mol at high coverage. A similar trend was observed in Figure 1.2.

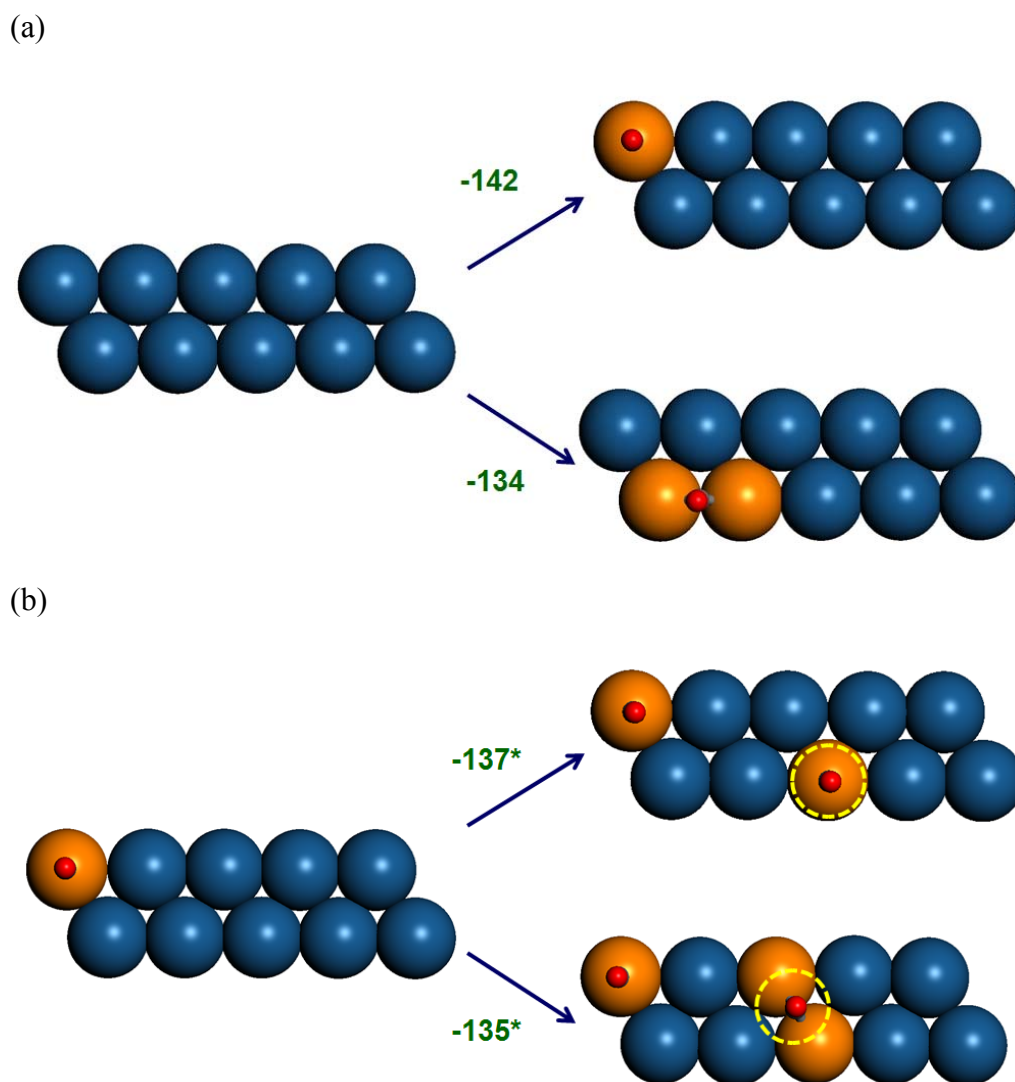
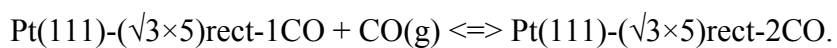


Figure 4.8 (a) CO adsorption energies for top and bridge sites at 1/10 ML coverage (b) Differential CO adsorption energies for top and bridge sites at 2/10 ML coverage.

Differential adsorption energies are calculated as follows,



Interestingly, CO becomes significantly less stable at the top site but gains stability at the bridge site when the coverage is increased from 1/10 ML to 6/10 ML (Figure 4.9). Likely, through space repulsion plays an important role in this and needs to be evaluated. To analyse a potential electronic origin, Bader charges and NBO occupancies were computed for the top and bridge sites. The Bader charge of the 2 Pt atoms which constitute the bridge site remains largely unchanged from a clean slab charge, while the Pt atom which constitutes the top site gains 0.01 electrons. This is remarkable considering that backdonation to CO is slightly larger (0.20) than the donation to the Pt surface (0.19) (Figure 4.9).

Next, a NBO analysis (Table 4.7) was performed. The anti-bonding sigma Pt-C occupancy increases from 0.53 to 0.54 electrons for CO at the top site when the coverage increases, indicating an increase in Pauli repulsion. On the bridge site however, the occupancies of the two anti-bonding sigma Pt-C NBOs decrease from 0.48 to 0.47 electrons when the coverage increases from 1/10 to 6/10 ML. Note that an increase in occupancy of 0.01 electron typically correspond to a change in bond strength by 0.01 atomic units or 25 kJ/mol. The CO $2\pi^*$ occupancies remain unchanged with the increase in coverage.

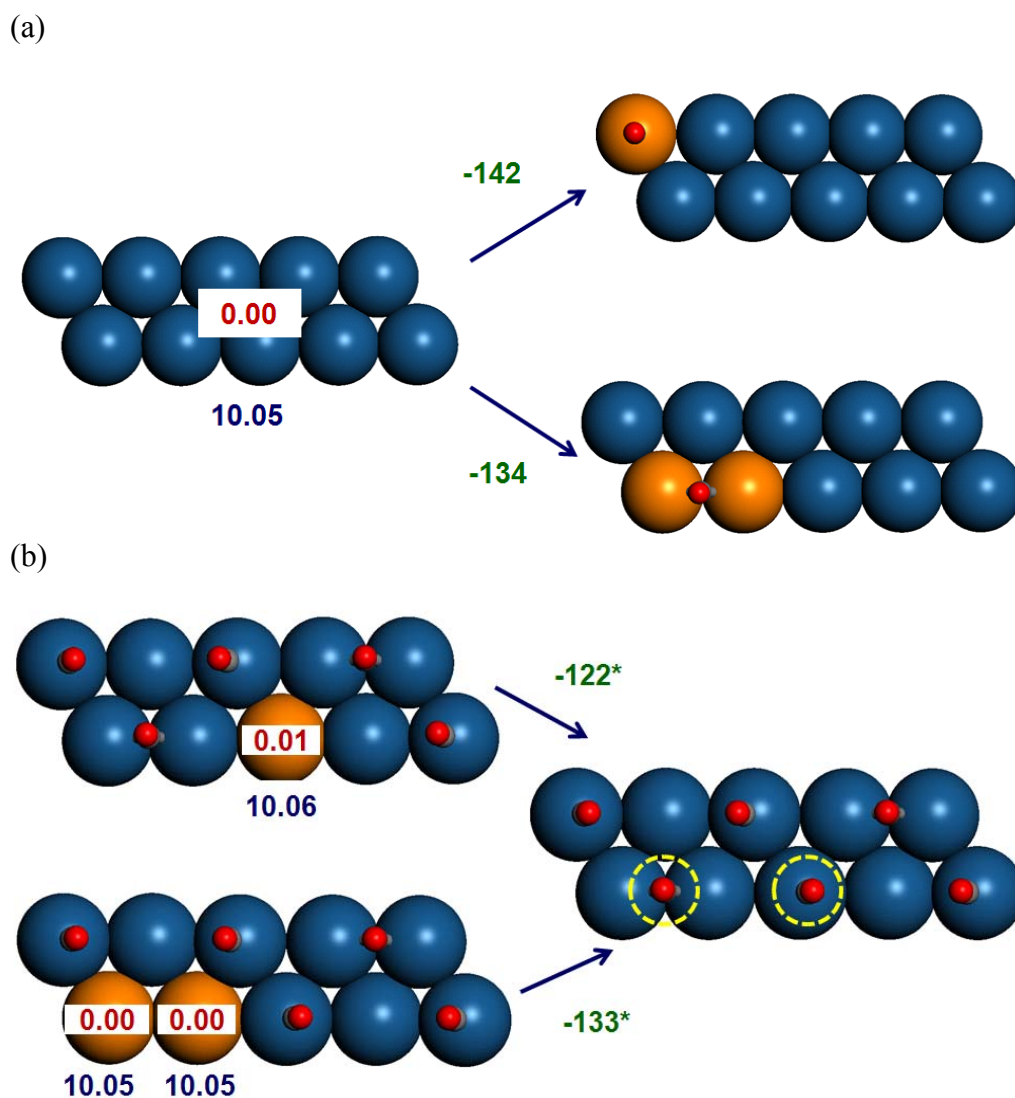


Figure 4.9 Change in the Pt(111)-($\sqrt{3}\times 5$)rect surface Bader charges (red: charge difference compared to neutral slab, blue: absolute valence charge) before CO adsorption (orange: the Pt atoms which CO binds) and adsorption energies (in green) are shown. (a) low coverage CO adsorption: the charge on the surface Pt atoms is slightly negative (0.05 excess electrons), as expected. (b) High coverage CO adsorption: the Pt atom, which constitutes the top site gain (0.01 excess electron) while the Pt atoms which constitute the bridge site remains unchanged compared to the clean slab charge.

Differential adsorption energies are calculated as follows,

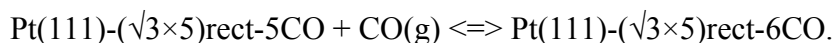


Table 4.7 Average and differential^a CO adsorption energies adsorption energies, occupancy of the anti-bonding Pt-C NBO and of the C-O 2 π^* NBO for 1/10 ML and 6/10 ML coverage CO structures on Pt(111)-($\sqrt{3}\times 5$)rect unit cell.

| Coverage | 1/10 ML - top | 1/10 ML - bridge | 6/10 ML - Persson et al. |
|--|---------------|---------------------|---|
| Adsorption energies (kJ/mol) | -142 | -134 | Top ^a : -122 Bridge ^a : -133 |
| Anti-bonding Pt-C NBO occupancy (electrons) | 0.53 | 0.48, 0.48 | Top: 0.54 Bridge: 0.47, 0.47 |
| CO 2 π^* NBO occupancy (electrons) | 0.20, 0.20 | 0.23 | Top: 0.20, 0.20 Bridge; 0.23 |

To further elucidate this trend, electrons were added (removed) to (from) the 5-layer $p(3\times 3)$ Pt(111) slab. The charge on the surface Pt atoms is slightly negative (0.05 excess electrons) for the neutral slab, while the central Pt atoms of the slab are slightly cationic, as expected. Addition of one electron to the 5-layer $p(3\times 3)$ slab (or 0.02 electrons per Pt atom) increases the charge of the surface Pt atoms by 0.04 electrons. In all calculations, more than 75% of the additional charge locates at the surface atoms, and less than 5% on the central atoms of the slab.

Table 4.8 Low coverage DFT-revPBE-vdW-DF CO adsorption energy as the charge of the surface Pt atoms changes in the 5-layer $p(3\times 3)$ Pt(111) slab.

| Surface charge per Pt (e) | CO adsorption energy (kJ/mol) | |
|---------------------------|-------------------------------|-------------|
| | Atop site | Bridge site |
| 0.00 | -160 | -142 |
| 0.05 | -143 | -136 |
| 0.09 | -132 | -135 |
| 0.13 | -120 | -132 |

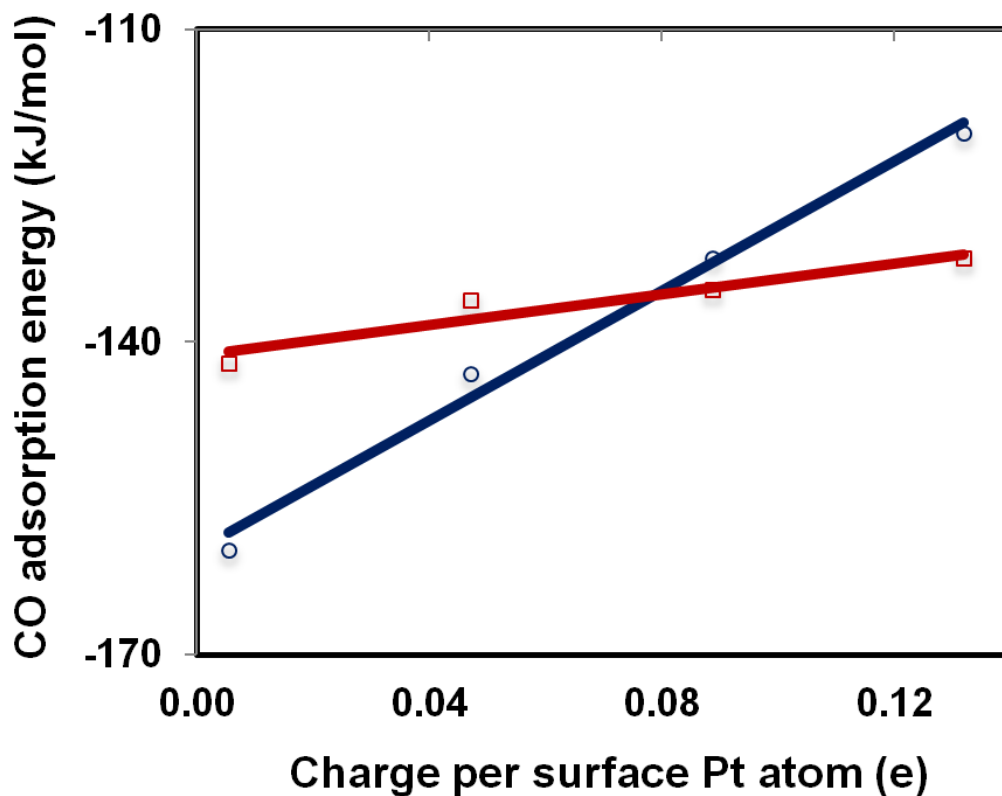


Figure 4.10 DFT-revPBE-vdW-DF CO adsorption energy, (■) bridge site (○) top site for 1/9 ML CO on Pt(111) as a function of the charge of the surface Pt atoms. The variation in the surface charge results from changes in the number of electrons in the 5-layer $p(3 \times 3)$ Pt(111) slab.

Figure 4.10 demonstrates that, CO at top sites are more sensitive to a variation of the surface Pt charge than CO at bridge site. A 0.04 e change in the charge of the surface Pt atom corresponds to a ~ 15 kJ/mol change in the adsorption energy for CO at top site.

4.3 Conclusions

CO adsorption on Pt(111) was studied with DFT-revPBE-vdW-DF. With this approach, the correct top site preference and accurate adsorption energies are predicted. In addition, the low coverage difference in adsorption energy (9 kJ/mol) between the top and the bridge sites nicely matches experimental estimates. As the coverage increases, the difference between the top and bridge stability reduces. The change in the relative stability for the top and bridge sites was analysed using the periodic implementation of NBO theory. Adsorption at both the top and the bridge site can be represented with classical Lewis structures with filled 2-center NBO's (>1.9). However, the corresponding anti-bonding orbitals also have significant occupancies (>0.1). At high coverages CO adsorption at the bridge site is energetically preferred over the top site. Although through space repulsion certainly contributes to this reversal in stability, the reduced electron density at the Pt atoms which constitute the bridge site reduces the Pauli repulsion, and increase the stability of CO at the bridge sites. The Pt atom which constitutes the top site however gains electrons and the adsorption energy at the top site decreases. With increase in coverage, several structures with very comparable stabilities are found, (4×2) -4CO [$(\sqrt{3} \times 2)$ rect-2CO], $(\sqrt{3} \times 5)$ rect-6CO, $(\sqrt{3} \times 3)$ rect-4CO. The stability of the various surface structures was analyzed using the changes in the occupancies of the NBOs, providing a quantitative analysis of the variation in the CO adsorption energy.

4.4 References

- [1] I. Langmuir, Transactions of the Faraday Society, 17 (1922) 621.
- [2] G.A. Somorjai, Y. Li, Introduction to Surface Chemistry and Catalysis, Wiley, 2010.
- [3] G. Ertl, M. Neumann, K.M. Streit, Surf. Sci., 64 (1977) 393.
- [4] H. Steininger, S. Lehwald, H. Ibach, Surf. Sci., 123 (1982) 264.
- [5] H. Hopster, H. Ibach, Surf. Sci., 77 (1978) 109.
- [6] J. Liu, M. Xu, T. Nordmeyer, F. Zaera, The Journal of Physical Chemistry, 99 (1995) 6167.
- [7] R.A. Shigeishi, D.A. King, Surf. Sci., 58 (1976) 379.
- [8] A. Crossley, D.A. King, Surf. Sci., 68 (1977) 528.
- [9] A. Crossley, D. A. King, Surf. Sci., 95 (1980) 131.
- [10] D.A. Kyser, R.I. Masel, Rev. Sci. Instrum., 58 (1987) 2141.
- [11] F. Thomas, N. Chen, I. Lee, L. Ford, P. Blowers, R.I. Masel, Journal of Vacuum Science & Technology A, 17 (1999) 2339.
- [12] W.T. Lee, L. Ford, P. Blowers, H.L. Nigg, R.I. Masel, Surf. Sci., 416 (1998) 141.
- [13] Y.Y. Yeo, L. Vattuone, D.A. King, The Journal of Chemical Physics, 106 (1997) 392.
- [14] W.A. Brown, R. Kose, D.A. King, Chem. Rev., 98 (1998) 797.
- [15] E. Schweizer, B.N.J. Persson, M. Tüshaus, D. Hoge, A.M. Bradshaw, Surf. Sci., 213 (1989) 49.
- [16] A. Cudok, H. Froitzheim, M. Schulze, Physical Review B, 47 (1993) 13682.
- [17] J. Yoshinobu, M. Kawai, Surf. Sci., 363 (1996) 105.

- [18] J.V. Nekrylova, I. Harrison, *Chem. Phys.*, 205 (1996) 37.
- [19] H. Froitzheim, M. Schulze, *Surf Sci.*, 211–212 (1989) 837.
- [20] W.D. Mieher, L.J. Whitman, W. Ho, *The Journal of Chemical Physics*, 91 (1989) 3228.
- [21] C. Papp, H.-P. Steinrück, *Surf. Sci. Rep.*, 68 (2013) 446.
- [22] M. Kinne, T. Fuhrmann, C.M. Whelan, J.F. Zhu, J. Pantförder, M. Probst, G. Held, R. Denecke, H.-P. Steinrück, *The Journal of Chemical Physics*, 117 (2002) 10852.
- [23] J.S. McEwen, S.H. Payne, H.J. Kreuzer, M. Kinne, R. Denecke, H.P. Steinrück, *Surf. Sci.*, 545 (2003) 47.
- [24] B.E. Heyden, A.M. Bradshaw, *Surf. Sci.*, 125 (1983) 787.
- [25] M. Tüshaus, E. Schweizer, P. Hollins, A.M. Bradshaw, *J. Electron. Spectrosc. Relat. Phenom.*, 44 (1987) 305.
- [26] A.M. Lahee, J.P. Toennies, C. Wöll, *Surf. Sci.*, 177 (1986) 371.
- [27] O. Björneholm, A. Nilsson, H. Tillborg, P. Bennich, A. Sandell, B. Hernnäs, C. Puglia, N. Mårtensson, *Surf. Sci.*, 315 (1994) L983.
- [28] F. Bondino, G. Comelli, F. Esch, A. Locatelli, A. Baraldi, S. Lizzit, G. Paolucci, R. Rosei, *Surf. Sci.*, 459 (2000) L467.
- [29] M. Kiskinova, A. Szab, J.T. Yates Jr, *Surf. Sci.*, 205 (1988) 215.
- [30] B.N.J. Persson, M. Tüshaus, A.M. Bradshaw, *The Journal of Chemical Physics*, 92 (1990) 5034.
- [31] N.R. Avery, *The Journal of Chemical Physics*, 74 (1981) 4202.
- [32] N.V. Petrova, I.N. Yakovkin, *Surf. Sci.*, 519 (2002) 90.
- [33] G. Nisbet, C.L.A. Lamont, M. Polcik, R. Terborg, D.I. Sayago, J.T. Hoefft, M. Kittel, R.L. Toomes, D.P. Woodruff, *Surf. Sci.*, 601 (2007) 1296.

- [34] K.L. Kostov, P. Jakob, D. Menzel, *Surf. Sci.*, 377–379 (1997) 802.
- [35] J.P. Biberian, M.A. Van Hove, *Surf. Sci.*, 138 (1984) 361.
- [36] Y.Y. Yeo, A. Stuck, C.E. Wartnaby, D.A. King, *Chem. Phys. Lett.*, 259 (1996) 28.

Chapter 5

Analysis of the change in the CO oxidation rate over Pt clusters by changing the charge transfer from the TiO₂ Anatase support

5.1 Introduction

In a detailed study, Chua et al. [1, 2] investigated the variation in the CO oxidation rate over a series of Pt catalysts supported on polycrystalline thin films of anatase TiO₂ with different carrier densities. The anatase films were synthesized to provide a controllable and well-characterized variation of about an order of magnitude in the n-type carrier concentration. The present work investigates the effect of charge transfer to the Pt catalyst on the CO adsorption energy using DFT. DFT calculations show that increased charge transfer to the Pt particles reduces the CO adsorption energy, but has only a

minor effect on the O adsorption energy. The measured changes in the reaction rate are consistent with the calculated changes in the CO affinity.

To evaluate the possibility of mass transfer limitations under the experimental conditions by evaluating the measured effective activation energy, CO oxidation experiments were carried out for a range of temperature. Reaction rates were measured for excess O₂ (1200 Pa) and limiting CO (10 Pa) conditions.

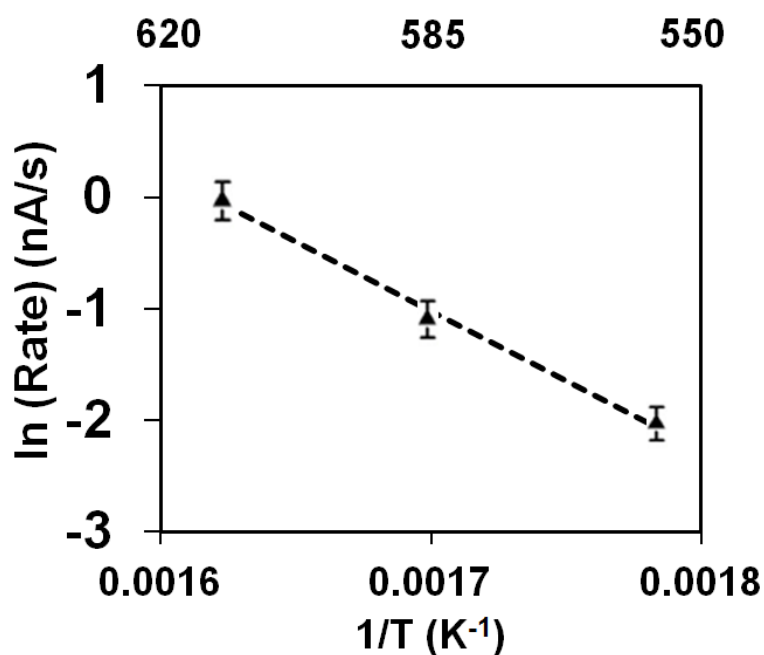


Figure 5.1 Arrhenius plot of the CO oxidation rate under excess O₂ (1200 Pa) and limiting CO (10 Pa) conditions for reaction temperatures of 560, 590 and 615 K.

The measured activation energy of 104 kJ/mol is in good agreement with activation energies reported by the group of Iglesia et al. [3, 4], of 80 to 120 kJ/mol, indicating that the experiments in our reactor setup and under these

conditions are under kinetic control and that mass transfer limitations, if any, have a limited effect on the measured rates. Indeed, if the measured rate was diffusion controlled, the temperature effect would be very different.

As discussed in Section 1.3, CO oxidation experiments were carried out in the Saeys group [1, 2] to evaluate the effect of changes in the anatase TiO₂ carrier concentration on the activity of small supported Pt particles. Reaction kinetics were measured in a low-pressure batch reactor (as explained in [1]) for both excess O₂ (1200 Pa) and excess CO (1200 Pa) conditions and under kinetic control, as demonstrated earlier.

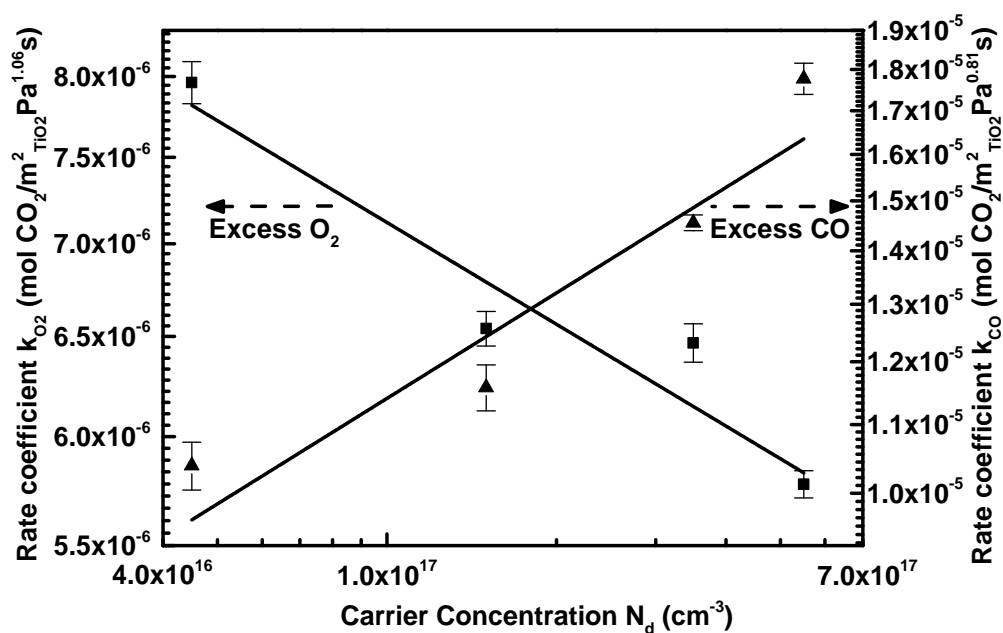


Figure 5.2 Effect of the anatase TiO₂ carrier concentration (N_d) on the CO oxidation rate coefficients for excess CO conditions (k_{CO} , \blacktriangle), and for excess O₂ conditions (k_{O_2} , \blacksquare). The lines presented in the figure are linear fits. Adapted from [2].

The variation of the reaction rate coefficients with the TiO₂ carrier concentration N_d is shown in Figure 5.2. Note that the variation in the *effective*

rate coefficient reflects changes in both the elementary rate coefficients and in the surface coverage [5]. For excess O₂ conditions, the effective rate coefficient k_{O_2} *decreases* by about 30% from 7.96×10^{-6} to 5.78×10^{-6} mol CO₂/m²_{TiO₂} Pa^{1.06} s as the carrier concentration increases from 4.5×10^{16} cm⁻³ to 5.5×10^{17} cm⁻³. In contrast, for the excess CO conditions the effective rate coefficient k_{CO} is more sensitive to the carrier concentration N_d and *increases* by about 70% from 1.04×10^{-5} to 1.78×10^{-5} mol CO₂/m²_{TiO₂} Pa^{0.81} s over the same range of carrier concentrations. In both regimes, the rate coefficient is approximately proportional to $\log(N_d)$. The CO oxidation rate coefficients hence change gradually by 30% and 70% when the TiO₂ carrier concentration changes by an order of magnitude, and the direction of the change depends on the limiting reactant.

To obtain a TOF from the measured rates, a Pt particle size was estimated. Using the particle size determined for a sputtering time of 5 s (3 nm) as an upper limit, a TOF of 430 s⁻¹ is obtained for a CO pressure of 120 Pa and a O₂ pressure of 1200 Pa. Assuming a smaller particle size of 1 nm (consistent with the shorter sputtering time of 1 s) reduces the TOF to 140 s⁻¹. Our TOF is somewhat higher than the value of 20 s⁻¹ obtained by extrapolating the data reported by Allian et. al. [3] at 423 K for Pt/Al₂O₃ to our conditions. Extrapolating the data reported by García-Diéguez et al. [4] at 713 K for Pt/Al₂O₃ to our conditions gives a value of 110 s⁻¹.

5.2 Computational methods

The computational methods used in this chapter are similar to the approach described in Chapter 2. However, instead of the recent revPBE-vdW-DF functional we used the revised Perdew-Burke-Ernzerhof functional (DFT-revPBE) [6] without vdW correlation in this earlier study. The optimized Pt lattice constant is 3.976 Å (experimental value: 3.92 Å) instead of 4.02 Å with revPBE-VdW. The effect of charge transfer to the Pt catalyst was modelled by changing the number of electrons in the slab. A large inter-slab spacing of 25 Å was used together with a dipole correction [7] to minimize interactions between repeated (charged) slabs. With these settings, adsorption energies were converged to within 5 kJ/mol. Also for charged slabs, the calculated adsorption energies changed by less than 5 kJ/mol when the inter-slab spacing was increased further.

5.3 Computational results

To model the effect of charge transfer from the TiO₂ support to the Pt catalyst, electrons were added (removed) to (from) the 5-layer $p(3\times 3)$ Pt(111) slab. The charge on the surface Pt atoms is slightly negative (0.05 excess electrons) for the neutral slab, while the central Pt atoms are slightly cationic, as expected. Addition of one electron to the 5-layer $p(3\times 3)$ slab (or 0.02 electrons per Pt atom) increases the charge of the surface Pt atoms by 0.04 electrons to 0.09 electrons. In all calculations, more than 75% of the additional charge locates at the surface atoms, and less than 5% on the central atoms of the slab.

CO and oxygen adsorption energies on Pt(111) slabs were calculated to study the effects of charge transfer on the adsorbate adsorption. For the neutral slab, both the low coverage (1/9 ML) CO adsorption energy at the top sites (-147 kJ/mol) and oxygen adsorption energy at the hollow sites (-356 kJ/mol) agree with the low coverage experimental values of -145 kJ/mol [8] and -360 kJ/mol, respectively [9]. Low coverage (1/9 ML), CO and oxygen adsorption energies are shown in Table 5.1 and Figure 5.11.

Table 5.1 Low coverage DFT-revPBE CO adsorption energy, O adsorption energy, CO stretch frequency as the charge of the surface Pt atoms changes. The variation in the surface charge results from changes in the number of electrons in the 5-layer $p(3 \times 3)$ Pt(111) slab.

| Surface charge per Pt (e) | Adsorption energy (kJ/mol) | | CO stretch frequency (cm^{-1}) |
|------------------------------|----------------------------|--------|--|
| | CO | Oxygen | |
| 0.005 | -165 | -357 | 2087 |
| 0.027 | -155 | -356 | 2070 |
| 0.047 | -147 | -356 | 2049 |
| 0.068 | -142 | -356 | 2017 |
| 0.089 | -139 | -356 | 1986 |

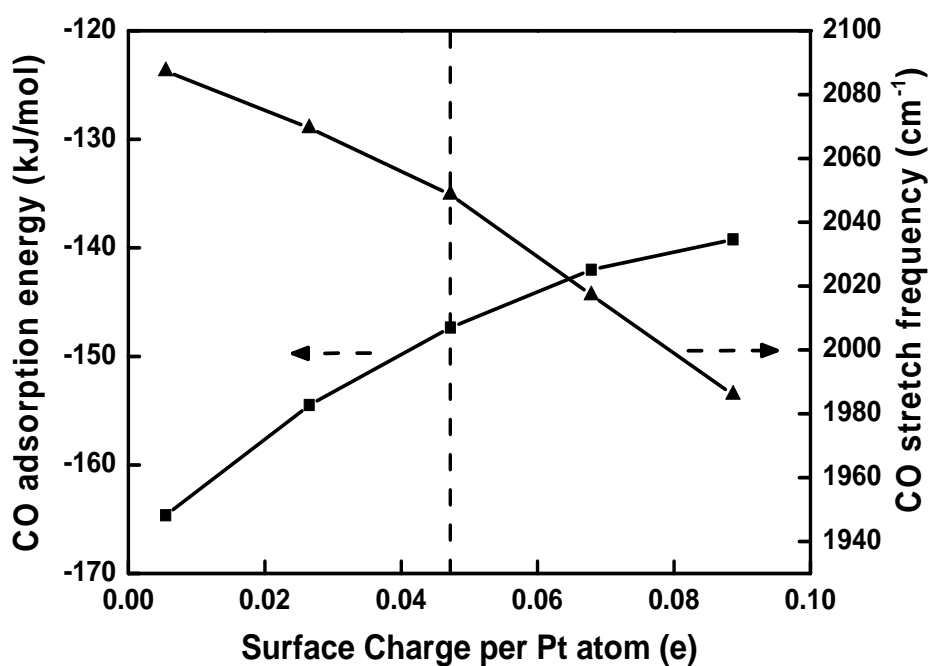


Figure 5.3 (a) DFT-revPBE CO adsorption energy (■) and C-O stretch frequency (▲) for 1/9 ML CO at the top side of Pt(111) as a function of the charge of the surface Pt atoms. The variation in the surface charge results from changes in the number of electrons in the 5-layer $p(3 \times 3)$ Pt(111) slab. The neutral slab is indicated by a dotted line and corresponds with a surface charge of 0.05 electrons/Pt atom.

The increased surface charge weakens CO adsorption by 8 kJ/mol (Figure 5.3). Over this limited range, the effect of charge injection on the CO adsorption energy is approximately linear. Removing one electron reduces the charge on surface Pt by 0.04 electrons and strengthens CO adsorption by 17 kJ/mol. The oxygen adsorption energy was found to be much less sensitive to charge transfer than the CO adsorption energy and changes by less than 2 kJ/mol when the surface charge per Pt atom increases from 0.005 to 0.089 electrons/Pt.

Under high CO pressure conditions, the catalysts surface should be covered with CO*. Coverage effects may dominate and the charge transfer may occur between Pt clusters and the adsorbates (CO* and O*). In order to understand the effects of coverages and especially the potential effects of coverages on the charge transfer, high coverage CO adsorption was studied as well.

Interestingly, the change in the CO adsorption energy for a higher CO coverage of 1/3 ML and 1.0 ML is similar to the change for the low 1/9 ML coverage (Table 5.2). CO adsorption energy decreases for both high coverages by 7 kJ/mol when the surface Pt charge of the neutral slab increases by 0.04 electrons.

Table 5.2 High coverage DFT-revPBE CO adsorption energy as the charge of the surface Pt atoms changes.

| Surface charge per Pt (e) | CO adsorption energy (kJ/mol) | |
|------------------------------|-------------------------------|--------|
| | 1/3 ML | 1.0 ML |
| 0.005 | -129. | -68 |
| 0.027 | -121 | -62 |
| 0.047 | -114 | -57 |
| 0.068 | -110 | -53 |
| 0.089 | -107 | -50 |

The Blyholder model describes CO adsorption on transition metals as donation from the filled CO 5σ orbital to vacant Pt d_{z^2} orbitals and backdonation from filled Pt d-orbitals to the vacant CO $2\pi^*$ orbitals [10]. This picture also emerges from a NBO analysis (Figure 5.4) [11]. Electron injection into the Pt slab increases the Fermi level and increases the occupancy of the Pt-C antibonding NBO. The increased Pauli repulsion decreases the CO adsorption energy. The increased surface charge also increases backdonation to the CO $2\pi^*$ NBO, as shown in Fig. 5.4. This increases the C-O bond length and decreases the CO stretch frequency (Figure 5.3). Even though the increased backdonation stabilizes the adsorbed CO, it does not fully compensate for the increased Pauli repulsion. Overall, the CO adsorption energy on Pt(111) is calculated to decrease when the surface charge increases.

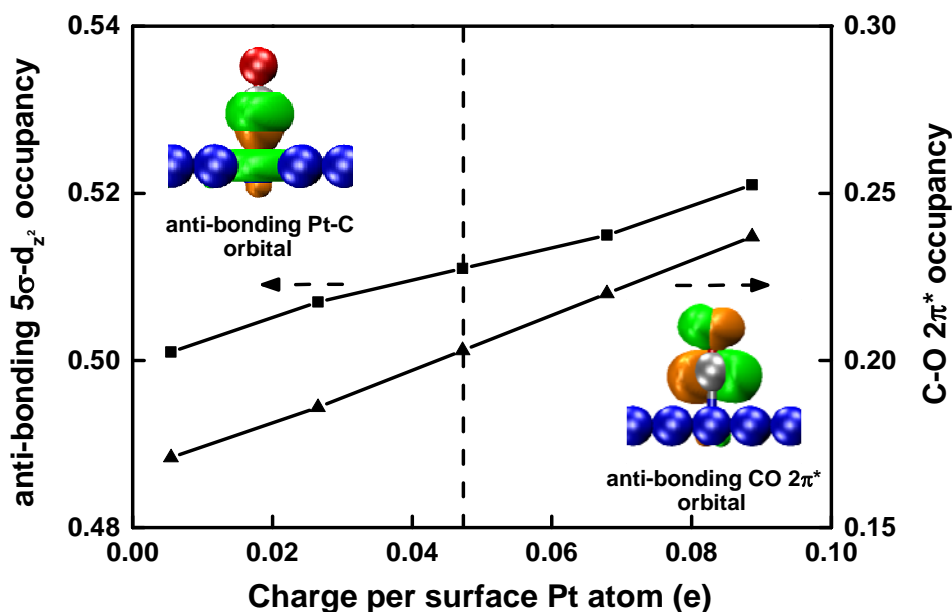


Figure 5.4 NBO analysis of the effect of charge injection on the calculated CO adsorption energy. Changes in the occupancy of the anti-bonding Pt-C NBO (■) and the C-O $2\pi^*$ NBO (▲) are shown. The variation in the surface charge results from changes in the number of electrons in the 5-layer $p(3\times 3)$ Pt(111) slab. The neutral slab is indicated by a dotted line and corresponds with a surface charge of 0.05 electrons/Pt atom.

In the series of supported Pt/TiO₂ catalysts, the order of magnitude change in the carrier concentration increases charge injection from 0.002 to 0.008 electrons per Pt atom. Based on Figure 5.11, this would weaken CO adsorption by about 2 kJ/mol and decrease the CO adsorption coefficient K_{CO} by about 35% at 350 °C. Under excess CO conditions (1.2 kPa CO), the CO coverage is expected to be high and weaker CO adsorption enhances the measured reaction rate [3, 4], in agreement with the observed trend. Under excess O₂ conditions (0.01-0.1 kPa CO, 1.2 kPa O₂), the measured rate is found to increase with the CO partial pressure. Weaker CO adsorption then decreases the reaction rate, again consistent with the measured variation.

5.4 Conclusions

DFT calculations and NBO analysis were used to analyse the change in the CO oxidation rate. Using CO oxidation as a probe reaction, the order of magnitude increase in the TiO₂ carrier concentration is shown to increase the effective CO oxidation rate coefficient by 70% under excess CO conditions and decrease the effective rate coefficient by 30% under excess O₂ conditions. DFT calculations and NBO analysis demonstrate that charge injection into the Pt particles reduces the CO adsorption energy by increasing the Pauli repulsion between the filled CO 5σ and Pt d_{z²} orbitals, consistent with the trends in the measured reaction rates.

5.5 References

- [1] Y.P.G. Chua, PhD Thesis, National University of Singapore, Singapore (2013)
- [2] Y.P.G. Chua, G.T.K.K. Gunasooriya, M. Saeys, E.G. Seebauer, *J. Catal.*, 311 (2014) 306.
- [3] A.D. Allian, K. Takanebe, K.L. Furdala, X. Hao, T.J. Truex, J. Cai, C. Buda, M. Neurock, E. Iglesia, *J. Am. Chem. Soc.*, 133 (2011) 4498.
- [4] M. García-Diéguez, E. Iglesia, *J. Catal.*, 301 (2013) 198.
- [5] I. Chorkendorff, J.W. Niemantsverdriet, *Concepts of Modern Catalysis and Kinetics*, Wiley-VCH, 2007.
- [6] Y. Zhang, W. Yang, *Phys. Rev. Lett.*, 80 (1998) 890.
- [7] G. Makov, M.C. Payne, *Physical Review B*, 51 (1995) 4014.
- [8] H. Steininger, S. Lehwald, H. Ibach, *Surf. Sci.*, 123 (1982) 264.
- [9] J.L. Gland, B.A. Sexton, G.B. Fisher, *Surf. Sci.*, 95 (1980) 587.
- [10] G. Blyholder, *The Journal of Physical Chemistry*, 68 (1964) 2772.
- [11] B.D. Dunnington, J.R. Schmidt, *Journal of Chemical Theory and Computation*, 8 (2012) 1902.

Chapter 6

Conclusions and future work

6.1 Thesis conclusions

Adsorption is a critical first step in heterogeneous catalysis. In this thesis we used DFT with the recent implementation of the revPBE-vdW-DF functional to study CO adsorption on both Co and Pt terraces. CO on cobalt was selected due to its industrial importance in Fischer Tropsch Synthesis. Co catalysts provide high FT activity and selectivity towards long-chain linear hydrocarbons. CO on platinum was selected due to its importance in understanding CO oxidation in automotive exhausts and use as anode catalysts for direct methanol fuel cells. In general, CO on Pt is considered as a model system in the field of surface science. Despite the long history of CO adsorption studies, several questions remain.

First, CO adsorption on Co(0001) was studied. With the theoretical approach developed in this thesis, the correct top site preference and accurate adsorption energies are predicted. With increase in CO coverage, two stable phases were found. Remarkably, all the other phases are significantly less stable. At low coverage the $(\sqrt{3}\times\sqrt{3})R30^\circ$ -CO phase dominates, while at high coverage the $(2\sqrt{3}\times2\sqrt{3})R30^\circ$ -7CO phase dominates. These phases are separated by a first order phase transition. The temperature and pressure of the first-order phase transition agree well with available experimental data as shown in the (p_{CO}, T) phase diagram for CO adsorption on Co(0001). Note that the temperature and pressure at which the transition occurs depends critically on the change in entropy and the change in enthalpy. At coverages below 1/3 ML, the calculations suggest the formation of isolated $(\sqrt{3}\times\sqrt{3})R30^\circ$ -CO islands due to attractive interactions between neighbouring CO molecules. The stability of the various surface structures was analyzed using the changes in the occupancies of the NBOs, providing a quantitative analysis of the variation in the CO adsorption energy. Experimentally, phase transitions are characterized by a discontinuity in the physical properties and modern micro-calorimetric methods might be able to directly observe the predicted phase transition.

The situation is very different on the well-studied Pt(111) surface. Many surface structures have comparable stabilities and even for a given coverage, many competing structures exist. About 20 structure were evaluated using DFT-revPBE-vdW-DF and stable structures were found for 0.5 ML $\{(4\times2)\text{-}4\text{CO} [(\sqrt{3}\times2)\text{rect-}2\text{CO}]\}$, 0.6 ML $\{(\sqrt{3}\times5)\text{rect-}6\text{CO}\}$, 0.67 ML $\{(\sqrt{3}\times3)\text{rect-}4\text{CO}\}$ based on a stability diagram. At low coverage, the adsorption energy at

the top site, -143 kJ/mol, is 7 kJ/mol stronger than at the bridge site, in agreement with an estimate based on detailed experimental data. As the coverage increases, the difference between the top and bridge stability reduces, e.g., to 7 kJ/mol at 0.125 ML and reverses at 0.25 ML. The change in the relative stability for the top and bridge sites was analysed using the periodic implementation of NBO theory. For both the top and the bridge site Lewis structure with filled 2-center NBO's (>1.9) were found by NBO analysis. However, the corresponding anti-bonding orbitals also have significant occupancies (>0.1) and dominate bonding trends. At high coverage CO adsorption on the bridge site is energetically favoured compared to the top site. Reduced electron densities on the Pt atoms which constitute the bridge site reduce the Pauli repulsion at those sites, and increase the CO stability.

Finally, to elucidate the gradual variation in the CO oxidation rate over sub-1 nm Pt clusters with the carrier density of the TiO₂ support (the so called Schwab effect), the effect of charge transfer to Pt on the CO adsorption energy was studied in detail. Using CO oxidation as a probe reaction, the Saeys group has shown that the order of magnitude increase in the TiO₂ carrier concentration increases the effective CO oxidation rate coefficient by 70% under excess CO conditions and decreases the effective rate coefficient by 30% under excess O₂ conditions. DFT calculations and NBO analysis demonstrate that charge injection into the Pt particles reduces the CO adsorption energy by increasing the Pauli repulsion between the filled CO 5 σ and Pt d_{z²} orbitals, consistent with the trends in the measured reaction rates.

6.2 Suggestions for future work

6.2.1 CO adsorption on other transition metals

As mentioned earlier, predictions of the correct site preference and of accurate CO adsorption energies are important challenges for DFT. As we demonstrated in this thesis, the DFT-revPBE-vdW-DF approach seems to provide an accurate description of CO adsorption on Co and Pt. An important question could be whether this finding is indeed general and extends to other important transition metals such as Ni, Cu, Ru, Rh and to other molecules. Furthermore, the effect of this functional on the predicted kinetics should be studied in detail. E.g., when hydrogen-bonding interactions are important, the effect of vdW correlation is expected to be important.

6.2.2 Tuning the ethylene hydrogenation rate over Pt/Anatase catalysts via the Schwab effect

Though a Schwab effect was demonstrated for CO oxidation and elucidated by calculations, the calculations also demonstrated that not every molecule displays the same sensitivity to changes in the charge density. In particular, CO was found to be rather insensitive due to the balance between donation and backdonation.

Preliminary calculations showed that the adsorption energy of ethylene is much more sensitive to changes in the Pt surface charge density. The hydrogenation of double bonds is of course industrially important, and selectivity challenges are ubiquitous. Preliminary DFT calculations (Table 6.1)

show that di- σ ethylene (figure 6.1) adsorption is indeed very sensitive to the Pt surface charge and the adsorption energy changes much more than CO.

Table 6.1 Low coverage DFT-revPBE-vdW-DF di- σ ethylene adsorption energy as the charge of the surface Pt atoms changes. The variation in the surface charge results from changes in the number of electrons in the 5-layer $p(3 \times 3)$ Pt(111) slab.

| Surface charge per Pt (e) | Adsorption energy (kJ/mol) |
|---------------------------|----------------------------|
| 0.005 | -181 |
| 0.027 | -126 |
| 0.047 | -95 |
| 0.068 | -48 |
| 0.089 | -19 |

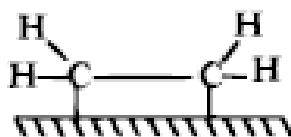


Figure 6.1 Schematic of a di adsorption mode of ethylene.

In addition, olefin conversion often suffers from CO poisoning. Rioux et al. [1] showed that ethylene hydrogenation over monodisperse Pt particles supported on silica are strongly affected by the presence of CO because CO competes with ethylene for the Pt active sites [1]. Tuning the charge on the Pt clusters supported on anatase TiO_2 could be expected to reduce the CO adsorption energy and reduce CO-poisoning of the ethylene hydrogenation reactions.

6.3 References

- [1] R. Rioux, R. Komor, H. Song, J. Hoefelmeyer, M. Grass, K. Niesz, P. Yang, G. Somorjai, *J. Catal.*, 254 (2008) 1.